Elsevier Editorial System(tm) for Ocean Modelling
Manuscript Draft

Manuscript Number:

Title: A multi-model study of the restratification phase in an idealized convection basin

Article Type: Full Length Article

Corresponding Author: Mr Clément Rousset,

Corresponding Author's Institution: LOCEAN-IPSL

First Author: Clément Rousset

Order of Authors: Clément Rousset; Marie-Noëlle Houssais; Eric P Chassignet

Abstract: The representation of baroclinic instability in numerical models depends strongly upon the model physics and significant differences may be found depending on the vertical discretization of the governing dynamical equations. This dependency is explored in the context of the restratification of an idealized convective basin with no external forcing. A comparison is made between an isopycnic model including a mixed layer (the Miami Isopycnic Coordinate Ocean Model, MICOM), its adiabatic version (MICOM-ADIAB) in which the mixed layer physics are removed and the convective layer is described by a deep adiabatic layer outcropping at the surface instead of a thick dense mixed layer, and a z-coordinate model (the French OPA model).

In the absence of a buoyancy source at the surface, the mixed layer geometry in MICOM prevents almost any retreat of this layer. As a result, lateral heat exchanges in the upper layers are limited while mass transfers across the outer boundary of the deep convective mixed layer result in an unrealistic outward spreading of this layer. Such a widespread deep mixed layer maintains a low level of baroclinic instability, and therefore limits lateral heat exchanges in the upper layers over most of the model domain. The behavior of the adiabatic isopycnic model and z-coordinate model is by far more satisfactory although contrasted features can be observed between the two simulations. In MICOM-ADIAB, the more baroclinic dynamics introduce a stronger contrast between the surface and the dense waters in the eddy kinetic energy and heat flux distributions. Better preservation of the density contrasts around the dense water patch maintains a more persistent baroclinic instability, essentially associated with the process of dense water spreading. The OPA simulation shows a faster growth of the eddy kinetic energy in the early stages of the restratification

which is attributed to more efficient baroclinic instability and leads to the most rapid buoyancy restoring in the convective area among the three simulations. Dense water and warm surface capping occur on a similar time scales. In MICOM-ADIAB, heat is mainly transported by anticyclonic eddies in the dense layer while both cyclonic and anticyclonic eddies are involved in the upper layers. In OPA, heat is mainly brought into the convective zone through the export of cold water trapped in cyclonic eddies with a strong barotropic structure. Probably the most interesting difference between the z-coordinate and the adiabatic isopycnic model is found in the temperature distribution ultimately produced by the restratification process. OPA generates a spurious volume of intermediate water which is not seen in MICOM-ADIAB where the volume of the dense water is preserved.

Suggested Reviewers:

Opposed Reviewers:

A multi-model study of the restratification phase in an idealized convection basin

Clément Rousset [a*], Marie-Noëlle Houssais [a], Eric P. Chassignet [b]

[a] LOCEAN-IPSL, UMR 7159, Université Paris 6, 4 Place Jussieu, Paris, France
[b] Center for Ocean-Atmospheric Prediction Studies, Florida State University, Tallahassee, FL, USA.

Submitted to *Ocean Modelling*

November 1, 2007

* Corresponding author address: LOCEAN-IPSL, UMR 7159, Université Paris 6, Boîte 100, 4 Place Jussieu, 75005 Paris, France.

Tel: (+33)1-44-27-70-71. Fax: (+33)1-44-27-38-05

E-mail address: clement.rousset@locean-ipsl.upmc.fr (Clément Rousset)

Abstract

The representation of baroclinic instability in numerical models depends strongly upon the model physics and significant differences may be found depending on the vertical discretization of the governing dynamical equations. This dependency is explored in the context of the restratification of an idealized convective basin with no external forcing. A comparison is made between an isopycnic model including a mixed layer (the Miami Isopycnic Coordinate Ocean Model, MICOM), its adiabatic version (MICOM-ADIAB) in which the mixed layer physics are removed and the convective layer is described by a deep adiabatic layer outcropping at the surface instead of a thick dense mixed layer, and a z-coordinate model (the French OPA model).

In the absence of a buoyancy source at the surface, the mixed layer geometry in MICOM prevents almost any retreat of this layer. As a result, lateral heat exchanges in the upper layers are limited while mass transfers across the outer boundary of the deep convective mixed layer result in an unrealistic outward spreading of this layer. Such a widespread deep mixed layer maintains a low level of baroclinic instability, and therefore limits lateral heat exchanges in the upper layers over most of the model domain. The behavior of the adiabatic isopycnic model and z-coordinate model is by far more satisfactory although contrasted features can be observed between the two simulations. In MICOM-ADIAB, the more baroclinic dynamics introduce a stronger contrast between the surface and the dense waters in the eddy kinetic energy and heat flux distributions. Better preservation of the density contrasts around the dense water patch maintains a more persistent baroclinic instability, essentially associated with the process of dense water spreading. The OPA simulation shows a faster growth of the eddy kinetic energy in the early stages of the restratification which is attributed to more efficient baroclinic instability and leads to the most rapid buoyancy restoring in the

convective area among the three simulations. Dense water and warm surface capping occur on a similar time scales. In MICOM-ADIAB, heat is mainly transported by anticyclonic eddies in the dense layer while both cyclonic and anticyclonic eddies are involved in the upper layers. In OPA, heat is mainly brought into the convective zone through the export of cold water trapped in cyclonic eddies with a strong barotropic structure. Probably the most interesting difference between the z-coordinate and the adiabatic isopycnic model is found in the temperature distribution ultimately produced by the restratification process. OPA generates a spurious volume of intermediate water which is not seen in MICOM-ADIAB where the volume of the dense water is preserved.

Keywords: Baroclinic instability; Convection basin; Model intercomparison; Restratification; Eddies; Idealized simulations.

1. Introduction

A large part of the deep water masses of the world ocean are formed in semi-enclosed basins (the Labrador Sea, the Greenland Sea or the Mediterranean Sea). Observations and numerical simulations conducted in these regions show that the convection can be divided into three phases: a preconditioning phase during which the cyclonic gyre-scale circulation rises isopycnals at the centre of the gyre, bringing the weakly stratified deep water close to the surface, which then appears as a thick homogeneous dense water lens underneath the relatively thin stratified surface layer; a mixing phase initiated by intense surface cooling which erodes the stratified surface water and, for a large enough buoyancy loss, makes it overturn in several plumes and rapidly mix to form a deep homogeneous convective patch; a restratification phase during which a new stratified water column occupying the upper and intermediate layers of the convective patch is established.

Two mechanisms contribute to the restratification, buoyancy added to the surface through heating from the atmosphere or sea ice melt water release, and lateral advection of buoyant stratified water from the periphery of the convective patch. When the mean circulation follows predominantly a circular path around the convective region, lateral exchange must occur primarily via mesoscale eddies generated through baroclinic instability of the mean flow (Morawitz et al. 1996). The process is efficient if a buoyant reservoir can be maintained at the periphery of the convective zone through, e.g., a warm boundary current (Lilly et al. 1999). After being restratified, the convective basin is capped by a light surface layer overlying a thick lens of dense homogeneous water, which is a remnant of the previous mixing event. The resulting stratification, especially the characteristics and the thickness of the upper stratified layer, depends upon the efficiency of the restratification processes and

ultimately determines the ability of the water column to be destabilized upon entering a new convection cycle.

The dynamics of the convection patch controls the restratification process. The instability builds on the potential energy stored in the front separating the outcropping dense, homogeneous water from the surrounding stratified waters, and, to a lesser extent, on the large scale kinetic energy associated with the rim current which flows in geostrophic balance along this front. Deformation of the mean cyclonic circulation pattern rapidly occurs in which the energy of the large scale flow cascades to smaller scale perturbations. If the radius of the mixed patch is greater than the Rossby deformation radius, the instability is mainly related to a baroclinic process in which the potential energy of the perturbations is converted into kinetic energy (Marshall and Schott 1999). Barotropic instability is also likely to occur, in relation to the horizontal shear of the rim current. Several eddies are formed which transport buoyant water from the surroundings to the interior whereas the cold dense water is exported from the convective patch towards the periphery. The role of the eddy fluxes in the restratification has been partially documented by observations in the different convective regions of the world ocean. These suggest that eddy fluxes alone could explain the restratification without the need for an additional buoyancy input from the atmosphere (Send et al 1995, Lilly et al 2003). From data collected in the 1990's, Lilly et al. (2003) estimated the eddy contribution to the lateral heat exchange between the boundary and the interior of the Labrador Sea to about 25%.

Analytical considerations together with numerical simulations and laboratory experiments have also demonstrated the central role of geostrophic eddies associated with the baroclinic instability of the rim current in controlling the restratification (Jones and Marshall, 1997).

Eddies are believed to constrain the restratification time scale as well as the characteristics of the end products and, provided the restratification operates during the mixing phase, the depth of the convective layer (Visbeck et al., 1996).

The representation of flow properties and the associated eddy field in numerical models is much dependent upon the model physics and most notably on the parameterization of the subgrid-scale processes (e.g. Willebrand et al., 2001). Major differences are thus seen when different coordinate systems are used to discretize the governing dynamical equations. In the ocean interior, far from regions of high mixing rates, transport and mixing preferentially occur along isopycnic surfaces while diapycnal mixing remains fairly low (Griffies et al., 2000a). The high ratio ($\sim 10^8$) of isopycnal mixing to diapycnal mixing is essentially guaranteed in isopycnic models where the two-dimensional transport equation is consistent with the adiabatic framework. As a consequence, isopycnic models are well known to better perform in tracking water masses. In the z-coordinate models, the advection schemes only guarantee numerical convergence to approximate adiabaticity and numerical truncation errors and horizontal diffusion introduce spurious diapycnal mixing which unphysically alters the characteristics of the advected water masses (Griffies et al., 2000b). The problem is particularly critical in z-coordinate eddy resolving models where a relatively high horizontal resolution, compared to what would be requested to simulate a realistic eddy field and to dissipate the accumulated variance and enstrophy at the cut-off grid scale, appears to be necessary in order to reduce the level of spurious mixing to small acceptable values (Griffies et al., 2000b).

Correlative to the different representations of advection and mixing are different characteristics of the hydrodynamic instabilities between isopycnic and z-coordinate models.

These differences have been investigated in idealized model configurations focusing on the stability of a jet like stream. When forced by an idealized wind stress, an eddy resolving isopycnic model shows a higher level of barotropic instability than its z-coordinate counterpart as a result of a higher level of mean kinetic energy (Bleck and Boudra, 1986). Additionally, the instability occurs earlier, as sharper horizontal density gradients can be sustained in absence of truncation errors and spurious horizontal mixing. The dominant instability in these experiments is however barotropic and is particularly sensitive to the mean kinetic energy distribution and thus to the subgrid scale parameterizations. Moreover, they address the particular case of a forced ocean in which the timing of the instability build-up is largely dependent upon the balance between forcing and dissipation. Additionally, the impact of truncations errors is probably overestimated due to the coarse vertical resolution of the models. By contrast, in buoyancy driven circulations such as those prevailing in convective regions, baroclinic instability should dominate and one may expect a sensitivity mainly controlled by the degree of baroclinicity of the flow and a greater sensitivity to the potential energy evolution.

The different developments of the baroclinic instability in two-layer isopycnic and z-coordinate simulations focusing on ring genesis and eddy cutoff processes have been investigated by Drifjhout (1992). He suggested that the choice of the advection scheme may be responsible for higher instability growth rates in the z-coordinate simulations due to the generation of spurious vorticity. The development of the instability was also shown to be sensitive to the amount of spurious diapycnal mixing, but the impact on the heat transport was more difficult to assess due to non linearities between viscosity and diffusivity effects. This aspect is a key issue when addressing the restratification of a convective basin, a process in which the eddy heat fluxes are the essential ingredient. Dedicated experiments using more

realistic configurations are needed in order to estimate these fluxes and better quantify their impact on the stratification of the basin in relation to the different model physics.

Although isopynic models are expected to perform better in an adiabatic fluid, the isopycnic representation is penalized in case of thick homogeneous layers such as deep convective mixed layers. In such cases, the model vertical discretization in the upper water column becomes insufficient to properly represent vertical contrasts, in particular current shears associated with density fronts (Eldevik, 2002). An example of such a limitation is found in the time evolution of the stratification in the Labrador Sea as simulated by the Miami Isopycnic Coordinate Ocean Model (MICOM) (fig. 1). After the end of the convective period (fig. 1a), the deep mixed layer (ML) is subject to rapid retreat. The retreat starts in mid-April (fig. 1b) but at that time is not related to a surface capping by surrounding lighter waters. Rather, the surface restratification is achieved through a one-dimensional rearrangement of the water properties during the ML retreat phase (fig. 1c) which, in this model, is essentially controlled by local heat and potential energy conservation requirements. A light surface layer that leaves a homogeneous 500 m thick intermediate layer underneath is not restored before the end of April. Additionally, by June, when the restratification has been completed, the volume of the dense water trapped underneath the upper stratified layers is larger than the volume initially available in the ML at the end of the convective period (compare fig. 1a and 1d). In contrast, observations at OWS Bravo during the same period show a gradual restratification of the intermediate water column until a rapid capping of the convected waters occurs by end of April (fig. 2). Concomitantly, the light surface layer experiences a salinity decrease (fig. 2b, bottom) which must have been triggered by advective processes. This is in contrast to the MICOM scenario in which surface warming dominates the early stage of the restratification. These observations suggest that the ML retreat in response to the surface buoyancy input from

the atmosphere is not the primary mechanism involved in the seasonal restratification of a convective basin. Lateral buoyancy exchange with the surroundings of the homogeneous region is the most probable mechanism for the seasonal restratification, a process that needs to be properly represented in models.

In order to investigate the impact of different model physics on the dynamics of the restratification in a convective basin, a typical case study has been analyzed based on simulations using models with different physics, but with a common experimental set-up (initial stratification and model forcing). Three models are considered, a z-coordinate model, an isopycnic coordinate model including a mixed layer, and a purely isopycnic model in which the surface layer is treated as an adiabatic layer in the same way as the other model layers. Our analysis focuses on relating the differences observed between the model simulations to the different representations of the mesoscale activity.

In section 2, a brief description of each of the three models is given including a discussion of selected physical parameters. In section 3, the models results are analyzed with a particular focus on comparing the kinetics and the efficiency of the restratification between the three models. In particular, diagnostics of the eddy activity in relation to instabilities are presented for the three models. A discussion follows in section 4 and a summary is finally given in section 5.

2- Numerical experiments

2.a Model physics

Three models are compared which all solve the three-dimensional hydrostatic primitive equations on a staggered horizontal C-grid with no-slip conditions at the solid boundaries. All

models are run with constant salinity. The primary difference between models is in the representation of the "vertical" coordinate. One of the models is a z-coordinate model (the OPA model, Madec et al., 1998) which, for the present analysis, includes a free surface on top. The stratification evolves through an advection-diffusion equation for the temperature (and, in the general case, the salinity). Viscous and diffusion processes are parameterized by second order diffusive operators with constant diffusion coefficients. A non penetrative convective adjustment scheme takes care of the hydrostatic instability.

The second model, the Miami Isopycnic Coordinate Ocean Model (MICOM 2.8, e.g. Bleck et al., 1992) is an isopycnic layer model capped by a vertically homogeneous non-isopycnal (i.e. density varying) ML which takes care of diabatic surface exchanges with the atmosphere (Bleck et al. 1989). The evolution of the thickness and hydrographic properties of the ML as a result of vertical mixing is predicted by an entrainment equation based on the Kraus-Turner (1967) formulation. Underneath the ML, the vertical stratification is described by discrete homogeneous isopycnic layers. There is no friction at the layer interfaces and interaction between layers only occurs through hydrostatically transmitted pressure torques. The stratification evolves due to changes in the individual layer thicknesses described by the continuity equation. Advection and diffusion of momentum and tracers occur along isopycnals. In our particular case study, the salinity is held constant. There is no mass transfer across isopycnals in the interior, except when prescribed (weak background in the experiments described in this paper). Mass transfer can occur between the ML and the underlying layers which are associated with the removal of hydrostatic instabilities arising at the base of the ML as a result of changes in the ML properties. Within the ML, advection and viscosity/diffusion of temperature and momentum are purely horizontal. Subgridscale mixing is parameterized by second order diffusive operators. A constant diffusivity is assumed for

scalar properties while, for momentum, a deformation dependent viscosity (Smagorinsky, 1963) is used.

Our comparative analysis includes a third model which has been designed to investigate the impact of the ML physics. This model (referred to as MICOM-ADIAB) is a "purely isopycnic" version of the MICOM model in which the ML physics are turned off and the surface layer is treated as a constant potential density layer in the same way as the underlying layers. In this particular version, except for a weak prescribed diapycnal flux, the mass of all individual layers are conserved.

2.b Experimental set-up

Three experiments using the three different models described above have been performed. All experiments are based on the same model domain and initial conditions with no external forcing. The domain consists of a flat bottom, circular basin of depth H_b = 1000 m and diameter 500 km (fig. 3a). The Coriolis parameter is constant and set to $f_0 = 10^{-4}$ s^{-1}. Salinity is maintained at a constant uniform value of 34.9 pss and the ocean density ρ only depends on temperature T. An equation of state is used in which the density is linearized around the initial bottom temperature using a thermal expansion coefficient of 1.95 10^{-4} $°C^{-1}$. For convenience, in the following, the model stratification will be described based on the temperature distribution.

The initial stratification is representative of conditions encountered at the end of a convective period in a typical subpolar convective basin (fig. 3b). A typical Labrador Sea stratification has been selected. At the centre of the basin, a vertically homogeneous cylinder of radius $R_c = 70$ km, filled with dense water of equivalent temperature $T = 4.86°C$, extends from the

surface down to H_c = 580 m (fig. 3a and b). This convective region is separated from a stratified domain by a 30 km wide front in which the horizontal temperature varies linearly. Over the the rest of the model domain, the vertical stratification is described by a horizontally uniform density profile corresponding to a constant buoyancy frequency $N = 1.9 \times 10^{-3} s^{-1}$. This stratification is representative of that encountered in the Labrador Sea boundary current if one excludes the very light Polar Surface Water (see, e.g., the AR7W sections in Pickart and Spall, 2007). The horizontal density gradient at the rim of the convective patch is also consistent with conditions encountered in the region. One should however notice that, since the salinity is held constant in our experiments, the temperature distribution cannot match the corresponding observed distribution. All models have 12 layers of thickness h_0 = 83.33 m which are equally spaced at the beginning of the experiment in all three models. The convective patch initially extends over the upper seven model levels in OPA or, alternatively in MICOM (resp. MICOM-ADIAB) is entirely contained in the ML (resp. the 7th layer of the model). It is important to note that in the particular experimental set-up used here, there is no mechanical or buoyancy source of turbulent energy at the surface and ML entrainment or retreat just cannot occur.

All models have the same horizontal resolution of 2.5 km which makes them eddy resolving in the more stratified water around the convective patch where the Rossby deformation radius, $L_d = \frac{NH_c}{f_0}$, is on the order of 10 km. In this definition of L_d, the depth of the convective patch H_c (rather than the total water column depth) is used, as the dynamical region is assumed to be concentrated along the density front, which mainly extends from the surface down to H_c.

Small values of the horizontal thermal diffusivity and viscosity (7.5 m^2 s^{-1}) are chosen so that the diffusion time scale across the basin (order of years) is large compared to the typical restratification time scale (order of days). Still, in the isopycnic models, the Smagorinsky scheme may be responsible for locally larger values of the viscosity. Vertical diffusion in OPA and diapycnal diffusion in the isopycnic models both amount to 10^{-5} m^2 s^{-1}. Diagnoses (not shown) of the respective contributions of diffusion and advection to the evolution of the temperature field show the strong predominance of the advection (both horizontal and vertical in OPA) over diffusion in all models. Diffusion is the largest in the frontal region at the rim of the convective patch where the isopycnals are steep and the horizontal temperature gradient strong. It contributes to about 10% of the three-dimensional heat exchanges in both OPA and MICOM-ADIAB but is dominated by the horizontal component in OPA and by the isopycnal fluxes in MICOM-ADIAB.

3. Results

3.a Evolution of the 3D temperature field

The analysis presented here focuses on the first months of the simulation, when the restratification process is the most active. Figure 4 shows the evolution of the stratification along a section across the centre of the basin. Figure 5 displays the evolution of the temperature distribution at 40 m and 290 m in OPA, and of the uppermost (k=1) and deep (k=7) layer thickness distribution in MICOM-ADIAB and MICOM. Except for MICOM, the last panels (day 100) in figure 4 show a state of nearly complete restratification after the dense water has spread from the centre out to the periphery of the basin, reforming a fairly uniform dense layer. Noticeable differences are seen in the vertical and horizontal distributions between the three models. In MICOM-ADIAB (fig. 4a), the surface of the convective patch is

capped by a thin layer of warm water with similar properties as water at the periphery. This surface capping does not reach the centre of the basin until day 30 and an intermediate restratification is not effective before day 45. In figure 5a, the meanders in the upper layers (top panel) occur on scales much larger than L_d and are likely to be destabilized through baroclinic instability of the front separating the dense water patch from the surroundings. The width of the front initially scales with three times the deformation radius characterizing the outer stratified region of the front, enabling a mixed barotropic/baroclinic (although soon to be predominantly baroclinic) instability. The lateral temperature gradient being the strongest in the uppermost layers, the capping of the convective region occurs primarily at the surface. Figure 4a also shows the persistence of a dense homogeneous water lens on day 100 which is the remnant of the initial dense water patch.

In OPA, the restratification is slightly faster than in MICOM-ADIAB (fig. 4c). On day 20, surface capping has already reached the centre of the domain and the intermediate restratification starts right afterwards. On day 100, contrasting with MICOM-ADIAB, the stratification of the basin is nearly uniform throughout the basin and the signature of the homogeneous dense water lens has almost disappeared. Intermediate waters are created to the detriment of the dense water. Meanders and eddies in figure 5c have scales comparable to those in MICOM-ADIAB but their domain of influence at depth extends further outward, consistent with the more efficient exchange in the intermediate layers.

In MICOM, neither the rapid surface capping by a thin warm layer nor a remnant convective layer underneath the surface layer are observed (fig. 4b). The convective patch is only slowly eroded from the sides by the surrounding warmer waters, leaving a still deep homogeneous water column at the centre of the basin after 100 days. On day 180 (not shown), this

homogeneous patch is slightly lighter but the restratification is still incomplete. Moreover, as the dense homogeneous patch laterally mixes with the surrounding intermediate layers, additional water incorporated into the ML leads to some ML deepening both in the centre and at the periphery of the patch. The meanders observed in the upper temperature field (fig. 5b) are associated with smaller horizontal scales and narrower lateral temperature gradients than in MICOM-ADIAB.

An important limitation of the MICOM model is the impossibility of ML retreat in absence of a buoyancy input from the atmosphere which, in the real world, would drive part of the restratification in the convective region. The resulting reformation of a seasonal ML then limits the vertical range over which the oversimplified homogeneous dynamics of the upper layer can be active. In the present MICOM experiment, lateral buoyancy exchange with the surrounding waters occurs uniformly over the entire depth range of the convective layer without the surface intensification needed for an efficient surface capping. In order to mimic a surface induced ML retreat, a sensitivity experiment has been performed, in which the MICOM model is initialized with the same density stratification as the standard one, but the initial ML depth is arbitrarily assumed to be uniformly equal to h_0 = 83 m throughout the whole model domain including the convective patch. While the initial buoyancy of the water column is kept unchanged, the thin initial ML leaves below it the most of the convected water. As a consequence, this water now occupies an isopycnic layer which will conserve its volume throughout the restratification process. The preservation of the dense water volume and properties is essentially what one would expect to happen once the light surface layer has capped the dense water patch. The experiment, however, is not entirely convincing as the lateral heat exchanges within the ML still induce some deepening of this layer in the vicinity of the temperature front. This deepening signal is propagated outward so that after a year, a

300 meter deep ML covers most of the basin. Moreover, while the ML characteristics in the centre of the basin are closer to the upper layer characteristics in the OPA or MICOM-ADIAB simulations, the ML is still too dense (temperature of 5.3°C instead of 5.8°C in MICOM-ADIAB). Buoyancy added to the surface layer would fix part of the problem.

3.b Time evolution of the buoyancy in the convective patch

The kinetics of the restratification in the different models can be estimated from the time evolution of the buoyancy of the convective patch. This evolution captures altogether the effects of the upper layer restratification and of the dense water spreading away from the centre of the basin. The buoyancy of the convective patch is calculated over a fixed volume cylinder with same lateral extent as the initial homogeneous cylinder and extending down to the bottom to accommodate the different geometry of the layers in the isopycnic and z-coordinate models:

$$B(t) = \frac{1}{V}\iiint_V (-\rho g)\,dV \qquad (1)$$

In (1), the integration is performed over the volume of a cylinder: $V = \pi R_c^2 H_b \sim 9\times10^3\, km^3$, g is the gravity and t is time.

Figure 6 represents the relative buoyancy change from the initial state, $\frac{B(t)-B(0)}{B(0)}$, in the three models. A fourth curve (dashed line) corresponding to the imposed retreat experiment is also plotted. A restratification time scale is difficult to estimate in MICOM as the buoyancy of the convective patch is still evolving after a year, indicating incomplete restratification. The timing of the restratification is not very different between OPA and MICOM-ADIAB

although the restratification occurs slightly faster in the former simulation, with a characteristic time scale of 70 days compared to 80 days. This is in agreement with the qualitative conclusion drawn from figure 4.

Since all experiments are unforced, the ultimate buoyancies characterizing the restratified convective patch on day 100 (fig. 4) is an indicator of the efficiency of the lateral eddy heat fluxes. In particular, the slightly larger buoyancy in OPA suggests a larger convergence of the heat transport into the convective zone. In MICOM, lateral advection across the density front at the outer boundary of the deep ML is probably not as efficient to transfer heat from the outer part of the domain into the interior, leading to much lower final buoyancy. The predominant role of the mixed layer is also evidenced in the "imposed ML retreat" simulation. Prescribing an initially shallow ML slightly improves the early stages of the simulation but, as in the standard MICOM simulation, the buoyancy does not stabilize and remains fairly low compared with the other two models.

The above differences between OPA and MICOM-ADIAB are likely to be related to the different heat advection schemes between the two models in relation to the different "vertical" coordinate. Additionally, they may also be the result of different levels of instability of the rim current. This level can be estimated from the restratification time scale as given by Jones and Marshall (1997) theoretical expression which, once reformulated for the case of a front wider than the deformation radius (Katsman et al., 2004), takes the form :

$$\tau_{restrat} = \frac{3}{2c_e}\frac{L_f}{L_d}\frac{R_c}{NH_c} \qquad (2)$$

in which L_f is the front width (here equal to 30 km) and c_e is a constant measuring the efficiency of the eddy transfers across the front. The associated values of c_e are 0.040 in MICOM-ADIAB and 0.047 in OPA. Both values are very close to the theoretical value of 0.045 deduced by Spall and Chapman (1998) from considerations on eddy dynamics within the assumption of uniform potential vorticity. More generally, they both fall in the range of values reported in the literature and based on numerical experiments simulating the restratification of a convective basin. Jones and Marshall (1997) deduced a value of 0.027 for c_e from an estimate of the restratification time scale; Spall and Chapman (1998) deduced values in the range 0.03-0.046 from eddy heat fluxes diagnosed in unforced numerical experiments. If the estimate of c_e is rather based on a diagnosis of the equilibrium density anomaly or chimney depth in response to surface forcing, similar values for c_e are found. Combining numerical and laboratory experiments, Visbeck et al. (1996) estimate a range of values between 0.014 and 0.056 while Spall and Chapman (1998) estimate is between 0.019 and 0.028. Examining regimes beyond the narrow front approximation where the ratio of the front width to the deformation radius is greater than 1 (like in our present simulations), Katsman et al. 2004 estimated a value of c_e = 0.02 based on the evolution of the buoyancy in the vicinity of the rim current during the restratification period.

The level of baroclinic instability is expected to decrease with horizontal model resolution. This is in agreement with lower value of c_e (0.028) found in a simulation using MICOM-ADIAB with 5 km resolution. Decreasing the resolution to 5 km slowed down the restratification in both OPA and MICOM-ADIAB, though without greatly altering the final buoyancy of the convective patch (not shown). Additionally, as the resolution becomes coarser, the difference between the restratification time scales in the two models becomes

larger (80 days in OPA compared with 120 days in MICOM-ADIAB) suggesting that the representation of baroclinic instability is more sensitive to the model physics when the internal radius of deformation is not adequately resolved.

3.c Distribution of the upper, intermediate and deep waters

The evolution of the water mass distribution has been investigated based on the evolution of the volume of each isopycnic layer inside (solid lines with left axis) and outside (dashed lines with right axis) the convective patch (fig. 7). The temperature distribution in OPA and in the ML in MICOM has been interpolated using a heat conserving scheme so as to reconstruct an equivalent distribution based on the prescribed temperature of the adiabatic isopycnic layers. Since this redistribution is fairly artificial for a deep ML which mixes properties between several layers, the pseudo-volumes of the corresponding isopycnic layers are plotted as dotted lines in figure 7 until the ML has actually reached the characteristics of the isopycnic layer. Given this redistribution, the volume of the convected water in all models appears to be initially contained in the 7^{th} layer. A somewhat arbitrary limit is introduced in the domain at a radius of 70 km to separate the "inner" volume contained within the initial convective cylinder from the "outer" volume. "Outer" volume variations should be exactly opposite to "inner" volume variations in a mass-conserving process. Note that the two volumes are normalized by the area of the inner domain so that "inner" volumes represent the actual layer thicknesses. The volume is divided into upper (layers 1-2), intermediate (layers 3-6), deep (layer 7) and bottom (layers 8-12) water masses.

At the end of the simulation, all models show a decrease of the deep water volume within the convective region in favour of an increase of the volume of the upper and intermediate water

masses. The decrease of the deep water volume within the convective region is the largest in MICOM. It is balanced by a corresponding increase of the intermediate water volume. The process is fairly slow since the ML characteristics do not reach those of the intermediate waters before day 120. The "inner" volumes of the upper water masses are about the same in OPA and MICOM-ADIAB, but the volume of the intermediate (resp. deep) water masses is larger (resp. smaller) in OPA. The characteristic time scales of the layer volume changes within the convective region are roughly the same for all layers in MICOM-ADIAB and OPA, except for the upper layers in OPA which start to reform only after some 20 days. This suggests that the restratification time scale is not different from the dense water spreading time scale. This time scale is however much shorter in OPA and most probably relates to the different baroclinic instability efficiency.

Diapycnal processes in OPA create altogether a substantial amount of intermediate waters and a slight amount of bottom water within the convective patch. The total (inner + outer) volume of the upper and deep layers in OPA indeed decreases (loss of 20 m and 330 m, respectively) while the intermediate layers gain mass. The comparison between the solid and dashed lines in figure 7 indicates that this mass gain almost exclusively occurs within the convective patch, without any compensating loss from the corresponding layers outside the patch. This suggests again that diapycnal processes must be involved, most probably via exchanges across the front separating the convective patch from the outer region. From the budget of the individual layers presented in figure 7, one can postulate that, overall, 340 meters of intermediate waters are created within the convective region from lateral exchanges between the deep water (for 250 meters) originally filling the convective patch and the upper (for 20 m) and intermediate (for 70 meters) waters from the outer region. An additional loss of 80 meters of deep water volume is due to diapycnal mixing with the bottom layers. By contrast "inner" volume

changes in MICOM-ADIAB are exactly compensated by "outer" volume changes. Diapycnal mixing is indeed negligible and stratification mainly changes through advection along isopycnals.

3.d Distribution of the kinetic energy and instabilities

In order to investigate the role of eddies in the restratification process, the distribution of the eddy kinetic energy (K_E) has been compared in the three simulations. In the definition of the mean and eddy components of the flow, a mass weighted average has been introduced which retains the information in terms of ocean layer thickness. For any variable $\psi(r,\theta,k,t)$, r being the radial distance to the centre of the basin, θ the azimuthal coordinate and k the layer index, this average can be written as $\tilde{\psi} = \overline{h\psi} / \overline{h}$, where $h(r,\theta,k,t)$ is the thickness of the k-layer and the overbar denotes spatial averaging. The associated fluctuations ψ' then verifies $\overline{h\psi'} = 0$. Note that h can be either the variable thickness of the layer in an isopycnic model or the constant level thickness, h_0, in a z-coordinate model, which in the latter case implies $\tilde{\psi} = \overline{\psi}$.

Figure 8 shows the horizontal circulation in the upper (0-83 m) and deep (500-583 m) layers on day 30. The radial symmetry of the initial stratification drives an upper cyclonic circulation and a deeper, weaker anticyclonic circulation around the convective patch which are subsequently broken up by instabilities and eddies. From figure 8, it appears reasonable to define the mean circulation based on an azimuthally averaged flow while the perturbed flow, defined as the deviation to this mean flow, should capture the effect of meanders and eddies. Consequently, the mean flow velocity is defined as:

$$\tilde{\bar{u}}(r,k,t) = \frac{\int_0^{2\pi} h\vec{u}d\theta}{\int_0^{2\pi} hd\theta} \qquad (3)$$

where $\vec{u} = (u_r, u_\theta)$ is the horizontal velocity, u_r and u_θ being its radial and azimuthal components. According to the flow geometry, one expects a mainly azimuthal fow verifying $\tilde{u}_\theta \gg \tilde{u}_r$.

The mean kinetic energy of a layer *k* of mean thickness $\bar{h}$ is:

$$K_M(r,k,t) = \frac{1}{2}\rho_0 \bar{h}(\tilde{u}_r^{\,2} + \tilde{u}_\theta^{\,2}) \qquad (4)$$

where ρ_0 is a reference density taken to 10^3 kg m^{-3}. The eddy kinetic energy is defined as the deviation from the mean:

$$\begin{aligned} K_E(r,k,t) &= \frac{1}{2}\rho_0 \overline{h(u_r^{\,2} + u_\theta^{\,2})} - K_M(r,k,t) \\ &= \frac{1}{2}\rho_0 \overline{h(u'_r{}^{2} + u'_\theta{}^{2})} \end{aligned} \qquad (5)$$

Figure 9 shows contrasted distributions of the eddy kinetic energy depending on the model. The energy level is much larger in OPA and MICOM-ADIAB than in MICOM which shows only a very limited region of substantial kinetic energy concentrated at the base of the ML. There, the isopycnic surfaces are the steepest and the evolution of the energy maximum shows an outward spreading following the evolution of the layer thickness gradients. Very little energy is found elsewhere, including in the ML. By contrast, in both MICOM-ADIAB and OPA, K_E is surface intensified. The radial structure of K_E in OPA shows several vertical

bands in which the energy decreases from the surface to the bottom. In MICOM-ADIAB, rather than a continuous feature in the vertical, a vertical dipole is found with a distinct extremum of energy at depth (~500 m), at the level where the dense water is expected to spread away from the convective region. The kinetic energy in the water column indeed appears to be concentrated along the tilted boundary separating the dense homogeneous water from the upper and intermediate stratified layers. In both models, the energy spreads both outward and inward at all depths but, in OPA, the eddy field extends farther outward than in MICOM-ADIAB.

Judging from figure 9, the eddy kinetic energy exhibits different time evolutions depending on the model. Averaged over the basin area, the energy does not reach a maximum before day 90 in MICOM while this maximum is reached earlier in the other two models. In both OPA and MICOM-ADIAB, the maximum indeed occurs on day 30 at the surface (fig. 10). Still, while OPA shows the same evolution of the kinetic energy throughout the whole water column, in MICOM-ADIAB the energy grows more slowly and more persistently at depth, reaching a maximum not before day 40.

In order to characterize the nature and the level of the instabilities leading to the eddy kinetic energy distribution seen in figure 9, the different contributions to the kinetic energy evolution have been estimated. Baroclinic instability builds on conversion of potential energy into eddy kinetic energy. Part of the potential energy of the mean large scale flow, P_M, is transferred to the eddy scales through a rearrangement of the mass field, thus creating eddy potential energy (P_E) which, in turn, is converted into kinetic energy. In P_M, we consider only that part of the mean potential energy (the so-called available potential energy or *APE*) which can be recovered for energy conversions. On the other hand, barotropic instability, which arises as a

result of horizontal shear in the mean flow, is associated with a conversion of mean kinetic energy (K_M) into eddy kinetic energy.

The reference state needed to estimate the *APE* is the state obtained after a complete adiabatic leveling of the isopycnal surfaces in which mass is conserved. In isopycnic coordinates, an estimate of the mean and eddy *APE* can be calculated from the displacements of the isopycnals relative to this horizontally uniform reference state (e.g., Houssais 1984), which for a layer interface *k* at a mean depth $\overline{z_k}$ can be written as :

$$P_M(r,k,t) = \frac{1}{2} g\Delta\rho_k (\overline{z}_k - z_{ref})^2 \qquad (6)$$

$$P_E(r,k,t) = \frac{1}{2} g\Delta\rho_k \overline{z'_k{}^2} \qquad (7)$$

where $\Delta\rho_k$ is the density jump across the interface, z_k' is the deviation of the interface depth from its mean and z_{ref} is the depth of the interface in the reference state. Alternatively, in a z-coordinate frame, direct estimate of the isopycnal displacements is no longer possible and the mean and eddy *APE* of a layer of fixed thickness h_0 are estimated as (e.g., Oort et al. 1989):

$$P_M(r,k,t) = \frac{1}{2} gh_0 \frac{1}{\partial\rho/\partial z\big|_{ref}} (\overline{\rho} - \rho_{ref})^2 \qquad (8)$$

$$P_E(r,k,t) = \frac{1}{2} gh_0 \frac{1}{\partial\rho/\partial z\big|_{ref}} \overline{\rho'^2} \qquad (9)$$

where $\left.\frac{\partial \rho}{\partial z}\right|_{ref}$ is the vertical density gradient in the reference state while $\overline{\rho}$ and ρ' are the mean density and the deviation from this mean at the *k*-level, respectively. In order to have consistent diagnostics, ρ_{ref} in OPA is deduced from a linear interpolation, onto the *k*-levels, of the isopycnal values defining the reference state in MICOM-ADIAB.

Figure 11 shows the mean, eddy and total kinetic and available potential energy averaged over the whole basin for the three models. We focus our attention here on the first 100 days of the simulations before dissipation processes lead to a general decrease of all types of energy. The large amount of potential energy (ca. 8000 J m^{-2}) initially stored in the steep isopycnals around the convective area is rapidly made available for conversion into kinetic energy. In all three models, the first days of the simulation bring out a fast geostrophic adjustment leading to a rim current around the convective patch (fig. 8). This adjustment is clearly identified in the production of mean kinetic energy to the detriment of the mean APE. At that time, K_M is about the same in OPA and MICOM-ADIAB (80-100 J m^{-2}) but is smaller in MICOM (40 J m^2). The following days are marked by a joint increase of the eddy potential energy and eddy kinetic energy. The growth of P_E is associated with an energy transfer from P_M but some of this energy production is converted into eddy kinetic energy through baroclinic instability contributing to the concomitant growth of K_E. In the early stages of the simulation, conversions between K_M and K_E through barotropic instability also contribute to the growth of K_E but these conversions are small when compared to the potential energy contribution. Judging from the evolution of K_M, the barotropic conversion is fairly continuous in MICOM while in OPA and MICOM-ADIAB, the initial conversion is followed by successive phases

of transfers between K_M and K_E which alternatively slow down or reinforce the growth of K_E.

In MICOM, the level of eddy kinetic energy is much smaller than in the other two models despite the high level of eddy potential energy. The slower growth of K_E is consistent with the evolution seen in figures 9 and 10. In fact, instead of the expected decrease, the potential energy of the whole system increases gradually, obviously in relation to the ML dynamics, but little of this energy reservoir is actually made available for baroclinic conversion into eddy kinetic energy. A careful examination of the different contributions to the potential energy increase reveals that half of it is due to the mass rearrangement associated with the ML deepening at the periphery of the convective patch while the other half is due to the export of dense water toward the periphery within the ML.

OPA and MICOM-ADIAB are close to each other in terms of eddy energy evolution. In particular, the two models maintain approximately the same level of eddy potential energy until day 40. A noticeable difference is however seen in the faster but less persistent growth of the eddy kinetic energy in OPA, which altogether maintains a higher kinetic energy level until day 60. More specifically, K_E grows faster during the first 25 days, reaching a maximum value of 1140 J m^{-2}, while in MICOM-ADIAB, a more persistent but slower growth takes place until day 40 when K_E reaches a maximum value of 850 J m^{-2}. As shown in figure 12, larger dissipation rates occur in MICOM-ADIAB during the first 25 days which certainly arise as the result of large flow deformation rates increasing the viscosity. Part of the reduced energy growth in MICOM-ADIAB during this early stage of the simulation may therefore be due to this larger dissipation rate and should not be entirely attributed to less efficient baroclinic conversions. During the following days, however, dissipation is very similar

between the two models (fig. 12) and the observed differences between the kinetic energy evolutions must relate to different production rates, essentially through a more persistent baroclinic instability in MICOM-ADIAB. The latter may be the result of the isopycnic model maintaining a higher level of potential energy when compared to OPA. During the first 40 days of the simulations, lower rates of potential energy dissipation (not shown) in MICOM-ADIAB combined with initially (before day 20) lower rates of conversion into kinetic energy indeed contribute to maintaining a higher level of potential energy in MICOM-ADIAB over that period. From day 40 onwards, potential energy dissipation rates are similar in the two models and the faster decrease of the eddy potential energy in OPA after day 40, which is concomitant with a faster decrease of the eddy kinetic energy, should be rather related to a slowing-down of the potential energy cascade from the large scale to the eddy scale. The fairly slow decrease of the mean potential energy in OPA during that period (fig. 11) is consistent with this scenario. By contrast, during the same period, the persistent decrease of the mean potential energy in MICOM-ADIAB suggests that the energy cascade is still active and able to maintain a high level of kinetic energy production through baroclinic instability.

An independent quantification of the strength of the instabilities can be obtained through estimates of the energy conversion rates which also help characterizing the nature of the instabilities. Some care must be taken in the calculation of the conversions involving the potential energy as the eddy potential energy calculated in isopycnic coordinates (eq. 6-7) is not directly comparable to that calculated in isobaric coordinates (eq. 8-9) (Bleck, 1985). In order to allow a consistent comparison between the conversion rates estimated in the two coordinate systems, Bleck (1985) proposed to not split the potential energy P into its mean and eddy components. Since direct exchange between P_M and K_E is not allowed in any coordinate systems, conversions from P to K_E can still be interpreted as conversions

between P_E and K_E. Additionnally, such a simplification allows one to ignore the details of the energy transfers from P to K_E which in isopycnic coordinates follow a slightly different pattern (involving the mean kinetic energy) from the one in isobaric coordinates as defined by Lorentz (1967) (see Bleck, 1985 for a more complete explanation).

Accordingly, the conversion rate from P to K_E can be written as:

$$C(P,K_E) = \rho_0(\overline{h\vec{u}'.\nabla_k.(\phi + p^*\alpha)} - \overline{\nabla_k.(h\vec{u}'\phi)}) \qquad (10)$$

while the conversion from P to K_M is:

$$C(P,K_M) = \rho_0(\overline{h\tilde{\vec{u}}.\nabla_k(\phi + p^*\alpha)} - \overline{\nabla_k.(h\tilde{\vec{u}}\phi)}) \qquad (11)$$

and the conversion from K_M to K_E is:

$$C(K_M,K_E) = -\rho_0\overline{h\vec{u}'.(\vec{u}'.\nabla_k)\tilde{\vec{u}}} \qquad (12)$$

in which $\alpha(k)$ is the specific volume of a k-layer, $\phi(k) = -g\rho_0\sum_{k'=1}^{k-1}\alpha(k')h(k')$ the geopotential, $p^*(k) = g\rho_0\sum_{k'=1}^{k-1}h(k')$ the depth of the upper interface of this layer in pressure units, and ∇_k is the horizontal gradient operator following this layer. To take into account the free surface, a correction is added to both ϕ and p^* so that:

$$\phi(k) = g\rho_0\left[-\sum_{k'=1}^{k-1}\alpha(k')h(k') + \alpha(k)z_{surf}\right](1+\eta) \qquad (13)$$

where z_{surf} is the sea surface elevation (positive downward) and η represents the barotropic correction to a baroclinic ocean:

$$\eta = \frac{\rho_0}{p_b^*}(gz_{surf} - M(1)) \qquad (14)$$

with *M(k)* being the Montgomery potential in the *k*-layer, and $p_b^* = \rho_0 g H_b$ the baroclinic pressure at the bottom.

In z-coordinates, the conversions terms can be expressed as:

$$C(P, K_E) = -gh\overline{w'\rho'} - gh\overline{\nabla.(\vec{v}'p')} \qquad (15)$$

$$C(P, K_M) = -gh\overline{w}\,\overline{\rho} - gh\overline{\nabla.(\vec{\bar{v}}\bar{p})} \qquad (16)$$

$$C(K_M, K_E) = -\rho_0 h\overline{\vec{u}'.(\vec{u}'.\nabla_z)\vec{\bar{u}}} \qquad (17)$$

where $\vec{v}$ is the three-dimensional velocity, *w* its vertical component, *p* is the pressure, and ∇ and ∇_z are the three-dimensional and horizontal (following the isodepths) gradient operator, respectively.

As already suggested by the evolution of the mean kinetic energy, the transfer from K_M to K_E in all three models is small compared to the baroclinic conversions involving potential energy (fig. 12). The radial distribution of the $C(K_M,K_E)$ conversion rate (not shown) shows that the barotropic instability occurs at the limit of the frontal region in all three models. In MICOM, the barotropic instability is the more active right at the mixed layer base where the isopycnic layer interfaces are the steepest and, therefore, the horizontal velocity shears are the largest. By contrast, in OPA and MICOM-ADIAB, similar vertical distributions of $C(K_M,K_E)$ are characterized by a surface intensified signal which oscillates in time. On the other hand, the evolution of the baroclinic kinetic energy production, $C(P,K_E)$, in both models shows a peak in the early stages of the simulation, followed by a period of rapid decrease until day 25. As expected, the two models however differ when considering the exact timing of the maximum energy production and longer term evolution. Although the maximum of the energy conversion rate has about the same value of about 1.5 10^{-3} W m^{-2} in both models, $C(P,K_E)$ in OPA the maximum is reached on day 6 and is followed by a slight decrease afterwards until day 12, while in MICOM-ADIAB, it occurs 6 days later on day 12. Integrating this conversion rate from the start of the experiment until the time of its peak value (day 12), a larger eddy kinetic energy production of 1250 J m^{-2} is indeed found in OPA compared with MICOM-ADIAB (900 J m^{-2}). On the other hand, after the period of rapid decrease (from day 25 onwards), the energy conversion shows larger persistency in MICOM-ADIAB than in OPA, as could be already anticipated from the joint evolution of the eddy energies in figure 11.

The ability of the flow to be destabilised through baroclinic instability and the likely preferred location of the instability can be further investigated using the Charney-Stern theorem (Charney and Stern, 1962) for quasi-geostrophic flows. In the case of a mean azimuthal flow,

the necessary condition for instability leads to the requirement that $\partial q/\partial r$ must change sign in any direction across the fluid, where q is the potential vorticity associated with the mean flow. For a mean flow with relative vorticity $\tilde{\varsigma}$ and mean thickness $\overline{h}$, the expression for q in isopycnic coordinates is :

$$q(r,k,t) = \frac{f + \tilde{\varsigma}}{\overline{h}} \qquad (18)$$

To make the layer expression of q (18) consistent with its z-coordinate counterpart $\frac{\partial \overline{\rho}}{\partial z}(f + \bar{\varsigma})$, q in figure 13 (a and b) has been multiplied by $\Delta\rho$, in which $\Delta\rho$ is the density jump between the isopycnic layers.

The locations of the strongest potential vorticity gradient are expected to coincide with regions of highest baroclinic production of kinetic energy. This matching is qualitatively verified for OPA in the intermediate layers upon comparing the vertical distribution of the local baroclinic production $-g\overline{hw'\rho'}$ (fig. 13d) with the distribution of the potential vorticity gradient (fig. 13c). The comparison also indicates that the surface energy production must be dominated by the contribution from transport of pressure anomalies which is not included in figure 13d.

Judging from figure 13, all three models show some persistent production of eddy kinetic energy at the periphery of the dense patch in agreement with the high levels of eddy kinetic energy there (fig. 9). As expected, in the isopycnic models where the potential vorticity is dominated by the stretching contribution rather than by the relative vorticity, the main regions

of baroclinic instability follow the geometry of the layers. In MICOM, no signs of baroclinic instability are seen within the ML where vertical shears cannot be resolved. In MICOM-ADIAB, however, large amounts of energy are being produced in the upper layer as a result of instabilities occurring along the upper interface of the dense layer and leading to the surface intensified signal in the K_E distribution (fig. 9). Changes in the vorticity gradient also occur within the dense water layer, at about 500 m, but somewhat later (see day 30, right panel) than at the surface. They are more localized, which is consistent with the slower energy growth at depth already noticed in the K_E distribution (fig. 9). In OPA, the energy production is associated with horizontal changes in the potential vorticity gradients which, although surface intensified, spread over the whole water column and persist throughout the main phase of the instability (left and right panels in fig. 13c).

3.e Lateral heat fluxes

The mean basin circulation being primarily azimuthal, the radial transport of heat must be achieved by eddies. Eddies carry heat into the convective patch and export cold water outside. The qualitative agreement between the time evolution of $C(P, K_E)$ and that of the buoyancy shown in figure 6, both suggesting more rapid restratification in OPA, demonstrates the crucial role of the baroclinic instability in the restratification process. For a layer of thickness *h*, the lateral eddy heat flux across the lateral boundary of a cylinder of radius r from the centre of the basin and unit height can be written as:

$$F(r,k,t) = \int_0^{2\pi} -u_r' T' r d\theta \qquad (19)$$

where u_r' is the eddy radial velocity component taken positive outward, and T' is the temperature fluctuation. In the two isopycnic models, as for the eddy kinetic energy, the vertical distributions of u_r' and T' are obtained through projection of the isopycnic velocity and temperature distributions onto a fixed z-coordinate framework.

In the two isopycnic models, the lateral eddy heat flux F is actually associated with a differential mass transport. In MICOM-ADIAB (fig. 14a), the differential is established between a surface (resp. deep) mass convergence and a deep (resp. surface) mass divergence inside (resp. outside) the convective patch. This differential represents the distinct processes of surface capping by formation of a new upper layer and deep water spreading. In MICOM (fig. 14b), the mass differential is inverted compared with MICOM-ADIAB, as the ML spreads outward and an inward mass flux fills the intermediate layers underneath the ML. This mass exchange is the only way for the model to handle the retreat of an originally deep mixed layer. Still, if the vertical integral is considered, these lateral mass fluxes are not the main contributors to the heat exchange (fig. 15 a and b). Diapycnal mass transfers associated with hydrostatic instability at the ML base, tend to redistribute vertically the advected anomalies. This redistribution dominates the deepening of the ML at the outer rim of the homogeneous patch (fig. 15b and d). Concomitantly, it opposes the retreat of the ML inside the patch (compare fig. 15a with 15b) and thus maintains a uniform ML base in this region which prevents inward penetration of the lateral eddy heat transfers associated with the ML depth gradients (fig. 15d). Lateral advection of temperature anomalies within the ML also contributes to the ML heat content evolution (fig. 15c). This latter contribution is smaller than the other two but, when considering the whole water column, it appears to dominate the overall warming (resp. cooling) of the convective (resp. outer) region (fig. 15c and e).

The differential mass transport in the two isopycnic models leads to the eddy heat flux distribution shown in figure 16a and b. Eddy heat fluxes in MICOM are mainly concentrated within the ML, but they are very small, consistent with the very slow changes in the ML properties observed in figure 4b. By comparison, MICOM-ADIAB exhibits the largest heat fluxes among the three models. The maxima have higher amplitude than in OPA, as a result of more persistent lateral density gradient in the isopycnic framework.

In all three models, the maximum of the lateral heat transfer follows the lateral boundary of the convective patch. In MICOM-ADIAB, two poles are clearly distinguishable. The inner one, aligned with the upper interface of the dense layer, is the stronger. The feature progressively extends further inward, representing the inward heat transport associated with the surface/intermediate restratification of the convective patch. A weaker, deeper pole in the outer region initially spreads across the 50-250 m layer but progressively deepens and moves outward. This deeper signal is associated with the upward displacement of the dense water interface in the outer region as a consequence of the outward spreading of dense water. In OPA, the initial two pole structure merges into a single enhanced signal at intermediate depth (~200 m). On day 30, most of the heat transfer occurs at intermediate depths, with a maximum still close to the rim of the dense patch, and the whole signal has extended outward over a somewhat greater distance than in MICOM-ADIAB. The absence of a distinct deep signal is consistent with the predominant reformation of intermediate layers diagnosed in figures 4c and 7 and attributed to the effect of diapycnal exchanges across the density front surrounding the convective patch.

Despite the larger lateral eddy heat fluxes in MICOM-ADIAB, the magnitude of the resulting heat flux convergence is very comparable to that in OPA (fig. 17). In OPA, vertical heat

transfers due to surface convergences (resp. divergences) occurring in cold (resp. warm) core eddies (not shown here), add some contribution to the surface warming. Additionally, downward (resp. upward) heat transport associated with downward (resp. upward) gradients of temperature anomalies induce an overall cooling from the surface down to 500 m. These vertical contributions are however smaller than the contribution from the horizontal exchanges. The resulting heat flux convergence must lead to a fairly uniform warming across the upper 500 m layer within the patch while it must cool this layer outside. In MICOM-ADIAB, the warming-cooling pattern has a vertically contrasted structure with the inward warming confined to the upper layers and the outward cooling concentrated in the intermediate and deep layers.

The time evolution of the vertically integrated eddy heat flux convergence indicates that the inward and outward spreading of the signal is very slow in MICOM so that little heat is actually transported away from the boundary of the convective patch (fig. 15e). In the other two models (fig. 17), the heating signal propagates inward at about the same rate during the first 10 days of the simulation and would ultimately reach the centre of the basin after about 35 days. However, after day 10, the spreading accelerates in OPA so that the heat fluxes already reach the centre of the basin on day 20. OPA also shows a more rapid cooling signal outside the convective patch than MICOM-ADIAB. The signal propagates over 70 km in 25 days while the same distance is performed in almost 35 days in MICOM-ADIAB.

The radial distributions of the eddy heat fluxes match the kinetic energy distribution shown in figure 9. In particular, the kinetics of the inward and outward spreading of the eddy kinetic energy away from the rim of the convective region is similar to that of the eddy heat flux. In the vertical, the matching is not as good in OPA. For instance, on day 30, larger eddy heat

fluxes occur at intermediate depths (~200 m) (fig. 16), most probably related to the strongest temperature fluctuations at that level, despite the eddy kinetic energy remains surface intensified (fig. 9). In MICOM-ADIAB, the distribution of the layer thickness fluctuations is expected to best correlate with the distribution of eddy kinetic energy, essentially through the vortex stretching of the mean flow which controls the regions of energy production. As a result, the model is able to maintain two extrema of the heat transport along the vertical which describe the distinct processes of surface capping and deep spreading. Isopycnic and z-coordinate models in fact generate eddy fields with somewhat different characteristics (fig. 18). In MICOM-ADIAB, the warm core anticyclonic eddies in the upper layers transport heat inward while the outside cooling is performed by cold core cyclonic (in the upper layers) and anticyclonic (in the deep layer) eddies (fig. 18a). In OPA, the eddy field tends to be more barotropic (fig. 18b), a feature which can be explained by secondary eddy induced circulations (Madec et al., 1991)**.** Lateral heat transport is therefore expected to be more uniform in the vertical although temperature gradients enhance the signal at mid-depth. At all levels, cold core cyclonic eddies are more efficient than warm core anticyclonic eddies in transporting heat from the outer region to the center of the basin. The horizontal distributions of the relative vorticity also show numerous occurrences of eddies shedding from the rim current toward the basin periphery in OPA (fig. 18b, left panels) which are not seen in MICOM-ADIAB.

4. Discussion

Bulk mixed layer models, such as the one included in the MICOM model, are known to perform reasonably well during the mixing phase of the convection, at least in the early stages when advection effects are not too important (e.g. Marshall and Scott, 1999). The present study shows that a bulk ML embedded in a three dimensional isopycnic model does not

adequately simulate the restratification phase in the absence of surface forcing, essentially because the physics of the lateral exchanges in the upper water column are not satisfactorily represented. One of the main shortcomings of these models is related to the fact that reformation of the light upper layers can only be achieved once the ML has itself reached the properties of these light waters, a condition which makes the process oversensitive to the timing and amplitude of the atmospheric surface buoyancy flux. When the latter is ignored as in the present study, purely horizontal advection/diffusion in the ML is unable to reconstruct the desired properties of the surface layers while persistent hydrostatic instabilities at the ML base prevent a dynamical retreat of this layer. As long as such a too deep ML persists, the vertical contrasts in the upper water column remain poorly resolved and the instability processes, yet known to play a crucial role in the first stages of the restratification, cannot be adequately represented. On the other hand, the domain where purely isopycnal physics are effective is restricted to the deeper, and therefore less dynamical layers underneath the ML. These conclusions are consistent with earlier model intercomparison studies focusing on frontal dynamics (Eldevik, 2002).

Among the three model physics explored, the adiabatic isopycnal physics shows the most realistic stratification at the end of the restratification period, allowing the persistence of a lens of convected dense water in agreement with observations (Send et al. 1995; Lilly et al. 1999). The distinct processes of surface capping and deep spreading are well reproduced in contrast to the z-coordinate model which shows unrealistic formation of intermediate water masses to the detriment of the dense water reservoir. Faster eddy kinetic energy growth rates or shorter restratification time scales such as those encountered in the z-coordinate simulations therefore should not be viewed as indications of a more efficient restratification.

The latter is more essentially dependent on the vertical distribution of the lateral eddy heat fluxes and therefore on the internal dynamics of the model.

The z-coordinate simulation indeed exhibits a somewhat higher maximum value of the eddy kinetic energy compared with the adiabatic isopycnic simulation. Diagnoses of the eddy activity in eddy-permitting models of the North Atlantic circulation have already pointed out higher levels of eddy kinetic energy in z-coordinate models (Willebrand et al., 2001 ; Barnier et al., 2001). The different levels of actual diffusivity and friction in the different models however made it difficult to draw a definite conclusion on the separate impact of the model physics. In the present OPA and MICOM-ADIAB simulations, similar parameterizations are used for diffusion and viscosity based on a Laplacian operator, and diagnosis of both tracer diffusion and eddy kinetic energy dissipation indeed reveal fairly similar domain-integrated values in the two models. Still, the deformation dependent friction in MICOM-ADIAB is responsible for local enhancements of the viscosity coefficient, and subsequent enhanced kinetic energy damping, in regions where the eddy activity is the largest (Willebrand et al, 2001). Even if this damping does not alter the general evolution of the eddy kinetic energy, it could indeed explain part of the difference in the level of K_E between MICOM-ADIAB and OPA during the first 25 days of the simulations.

Examination of the evolution of the source and sink terms in the kinetic energy equation over the entire active phase of the baroclinic instability shows that the different kinetic energy levels between MICOM-ADIAB and OPA are however mostly related to the different rates of eddy kinetic energy production, essentially through baroclinic instability. The latter indeed grows faster in the z-coordinate simulation, at least during the early, most active phase of the instability. Analyzing the non linear stage of the instability of a jet stream in idealized two-

layer model configurations, Drijfhout (1992) attributed the larger instability growth rates in the z-coordinate model to the generation of spurious vorticity due to an advection scheme which does not conserve potential vorticity. He also noticed that these differences in the growth rates did not impact on the eddy heat flux as the structure of the eddies is ultimately similar in the isopycnic and z-coordinate simulations. Our comparison indicates that some differences may indeed be found in the heat flux distribution as well. These differences may be attributed to the additional effect of spurious diapycnal mixing of momentum in the z-coordinate model. This effect was found by Drijfhout (1992) to increase the persistency of the wave breaking process as a result of the weakening of the vorticity gradients in the flow meanders, thus being responsible for larger heat fluxes. According to the same analysis, the different timing of the baroclinic instability between MICOM-ADIAB and OPA, with a maximum of the energy conversion reached earlier in OPA and a slower, more persistent energy conversion in MICOM-ADIAB, would reveal some sensitivity of our models to spurious diapycnal mixing of density, despite the relatively low value of the diffusivity coefficient. Increasing the vertical resolution in the z-coordinate model should reduce the overestimation of the level of instability (e.g., Ikeda and Wood, 1993), as well as of the eddy heat transport through reduction of the spurious diapycnal mixing of potential vorticity (Drijfhout, 1992). Apparently, the vertical resolution chosen in our experiments is not fine enough to entirely remove such spurious effects.

The restratification time scale, as estimated from the evolution of the buoyancy of the convective patch, is only slightly shorter in the z-model than in the isopycnic model (70 days versus 80 days) leading to fairly similar efficiency coefficients (0.047 versus 0.040). Taking MICOM-ADIAB as the more realistic simulation, we can estimate that about 80 % of the initial dense water volume has spread away from the convective patch in 60 days. During that

period the buoyancy in the patch increases almost linearly while afterwards, the increase slows down as the isopycnal gradients are progressively eroded. Based on this linear rate, the whole of the convected water would be exported in 75 days, which is very close to the flushing time which can be deduced from Khatiwala and Visbeck (2000) estimate based on observations in the Labrador Sea. These authors calculated a "flushing time" $\tau_f \approx 3.2$ years, which is the time necessary for a dense layer of thickness H = 1000 m and radius R = 200 km to spread away from the convective patch. Considering that, in our simulations, the dense water initially occupies a layer of thickness 580 m and radius 70 km, a simple proportional relationship to Khatiwala and Visbeck (2000) estimate would give a flushing time $\tau_f \approx 80$ days. This value is very close to the time scale estimated from the buoyancy change and suggests that, despite the highly idealized stratification in our simulations, the model dynamics in MICOM-ADIAB would be able to reproduce the basic kinetics of the ventilation of the Labrador Sea Water.

The three types of model analysed in this study show contrasted vertical and radial distributions of the eddy heat fluxes. In MICOM-ADIAB, these distributions are closely linked to the eddy kinetic energy distribution with the layer physics leading to a strong baroclinicity of eddies with the associated heat transports. The surface capping of the convective patch and the outward spreading of the cold dense water occur on similar time scales. Some observations in convective regions show a faster surface capping compared to the dense water spreading (Send et al. 1995; Lilly et al. 1999; Lilly et al. 2003). The discrepancy may be due to a damping effect in our unforced simulation as, in the real ocean, strong boundary currents contribute to maintaining lateral temperature gradients around the convective patch. In OPA, the more barotropic structure of the eddies leads to more vertically uniform heat exchanges but, still, those are more intense at intermediate depth than at the

surface, contrasting with the surface intensified structure of the kinetic energy. The vertical heat transfers associated with this eddy structure contribute to reestablish some baroclinicity by adding some surface warming and some deeper cooling. Yet this vertical redistribution has a limited effect on the stratification compared with the horizontal contributions. In MICOM, spurious features arise as the bulk of the adiabatic heat transport is constrained to accomodate the geometry of the mixed layer base in order to follow the thickness (or alternatively potential vorticity) gradients. Advection of surrounding water into the convective area therefore mainly occurs underneath the ML, but the reconstitution of the intermediate waters is greatly limited by hydrostatic instability which mixes these waters properties with those of the ML water. Although including a surface buoyancy source would certainly limit these processes through a control of the ML geometry, the associated reverse system of restratification/spreading, in which the dense water initially stored in the deep ML is advected outward at the surface rather than at depth, would still exist. Additionally, that the timing of the restratification be entirely controlled by the atmospheric buoyancy flux is not what is observed in the real ocean.

The predominance of anticyclonic eddies in MICOM-ADIAB is not observed in OPA. This predominance has however been observed and validated by simulations of the restratification period in the Labrador Sea using a sigma-coordinate model (Lilly et al., 2003). On the other hand, eddies appear to have comparable size in OPA and MICOM. Some comparative studies of the hydrodynamic instabilities in a z-coordinate model and an isopycnic model forced by wind stress have revealed a smaller sensitivity to lateral dissipation in the isopycnic model (Bleck and Boudra, 1986). Since dissipation in this study was parameterized by a scale selective biharmonic operator, these results suggest that the size of the eddies should be larger in the isopycnic model than in the z-coordinate model. Identifying such differences in our

simulations would require a detailed examination of the eddy characteristics which is beyond the scope of this study.

5. Summary and concluding remarks

To investigate the impact of different model behavior associated with the representation of the vertical coordinate on the restratification of a deep convective basin, a case study has been analyzed in simulations performed with three different models: a z-coordinate model, an isopycnic model including a ML, and a "purely isopycnic" model.

The baroclinic conversion of potential energy is the main source of eddy kinetic energy in both the z-coordinate and the isopycnic simulations. Both the z-coordinate model and the purely isopycnic model have many features in common. Global indicators like the restratification time scale and the associated instability efficiency are very similar. Still different spatial distributions and time evolutions of both the eddy kinetic energy and the eddy heat fluxes have been identified. At the beginning of the restratification period, the eddy instability grows faster in the z-coordinate simulation and the kinetic energy reaches a maximum after about 3 weeks. The energy conversion is however less persistent than in the purely adiabatic version of the isopycnic model where the peak value of the kinetic energy is not reached before 6 weeks. It is likely that these differences are inherent to the different model physics, and likely to be partly related to the spurious diapycnal mixing in the z-coordinate model which altogether amplifies the instability of the rim current and contributes to enhanced dissipation of the potential energy of the whole system.

In the purely isopycnic model, contrasted dynamics exist between the upper and dense layers. Warm anticyclonic as well as cold cyclonic eddies contribute altogether to the overall warming (resp. cooling) of the upper layers inside (resp. outside) the convective patch. The dense water spreading is essentially achieved by deep cold core anticyclones. The time scale of the surface capping and deeper spreading are identical. By contrast, in the z-coordinate model, heat is predominantly transported by cold core cyclonic eddies with a more barotropic structure. Spreading of dense water with unaltered characteristics is hardly identified. Rather, an overproduction of intermediate water occurs through diapycnal echanges across the density front surrounding the dense water patch. The warming signal is transported faster inward than the cooling signal is outward.

In the isopycnic model including a ML, the geometry of the ML and the absence of a continuous buoyancy source prevent any retreat of the deep ML in the convective patch. Inclusion of a mixed layer also leads to a weak eddy field with the smaller kinetic energy level among the three simulations. Part of these deficiencies would be certainly avoided by allowing vertical shear in the mixed layer like in the Hallberg isopycnic model (HIM, Hallberg and Rhines, 1996; Thompson et al., 2002) or by using a hybrid isopycnic-Cartesian coordinates ocean model like HYCOM (Bleck, 2002; Chassignet et al., 2003) in which the discretization of the ML in z-coordinate would greatly improve the physics of the upper layer.

Our analysis neglects the latitudinal dependency of the Coriolis parameter. According to the linear theory of baroclinic instability, this dependency should have a stabilizing effect on the flow field. It should also induce some westward displacement of the convective patch, altering its azimuthal symmetry and therefore the distribution of the lateral exchanges with the surroundings.

Acknowledgements

We would like to thank Alain Colin de Verdière, Christophe Herbaut, Patrice Klein, Gurvan Madec, Laurent Mortier and Anne-Marie Tréguier for fruitful discussions about the content of this paper. This work has been supported by the European FP6 project DYNAMITE (contract 003903-GOCE), and by the French project LIVINGSTONE (contract BLAN-NT05-2_43280, funded by Ecole Nationale Supérieure de Techniques Avancées, ENSTA). Computational ressources have been provided by the French Institut du Développement et des Ressources en Informatique Scientifique (IDRIS).

References

Barnier, B. et al., 2001. On the seasonal variability and eddies in the North Brazil current: Insights from model intercomparison experiments. Prog. Oceanogr., 48: 195-230.

Bleck, R., 1985. On the conversion between mean and eddy components of potential and kinetic energy in isentropic and isopycnic coordinates. Dyn. Atmos. Oceans, 9: 17-37.

Bleck, R., 2002. An oceanic general circulation model framed in hybrid isopycnic-Cartesian coordinates. Ocean Modelling, 4: 55-58.

Bleck, R. and Boudra, D., 1986. Wind-driven spin-up in eddy-resolving ocean models formulated in isopycnic and isobaric coordinates. J. Geophys. Res., 91: 7611-7621.

Bleck, R., Hu, D., Hanson, H.P. and Kraust, E.B., 1989. Mixed layer-thermocline interaction in a three-dimensional isopycnic coordinate model. J. Phys. Oceanogr., 19: 1417-1439.

Bleck, R., Rooth, C., Hu, D. and Smith, L.T., 1992. Salinity-driven thermohaline transients in a wind- and thermohaline-forced isopycnic coordinate model of the North Atlantic. J. Phys. Oceanogr., 22: 1486-1505.

Charney, J.G. and Stern, M.E., 1962. On the instability of internal baroclinic jets in a rotating atmosphere. J. Atmos. Sci., 19: 159-172.

Chassignet, E.P., L.T. Smith, G.R. Halliwell, and R. Bleck, 2003. North Atlantic simulation with the HYbrid Coordinate Ocean Model (HYCOM): Impact of the vertical coordinate choice, reference density, and thermobaricity. J. Phys. Oceanogr., 33: 2504-2526.

Eldevik, T., 2002: On frontal dynamics in two model oceans. J. Phys. Oceanogr., 32: 2915-2925.

Drijfhout, S.Y., 1992. Ring genesis and the related heat transport. Part II: A model comparison. J. Phys. Oceanogr., 22: 268-285.

Drijfhout, S.S., 1990. Eddy-genesis and the related transports of heat, momentum and vorticity; A parameter study. J. Phys. Oceanogr., 20: 1645-1665.

Griffies, S.M. et al., 2000a. Developments in ocean climate modelling. Ocean Modelling, 2: 123-192.

Griffies, S.M., Pacanowski, R.C. and Hallberg, R.W., 2000b. Spurious diapycnal mixing associated with advection in a z-coordinate ocean model. Mon. Weather Rev., 128: 538-564.

Hallberg, R., and P. Rhines, 1996. Buoyancy-driven circulation in an ocean basin with isopycnals intersecting the sloping boundary. J. Phys. Oceanogr., 26: 913-940.

Houssais, M.-N., 1984. Available Potential Energy for the Tourbillon Eddy: A Tentative energy Budget from the CTD Mesoscale Arrays. J. Phys. Oceanogr., 14: 1350-1364.

Ikeda, M. and Wood, R.A., 1993. Mesoscale stability of an ocean current in the Bryan-Cox model. J. Geophys. Res., 98: 12527-12536.

Jones, H. and Marshall, J., 1997. Restratification after deep convection. J. Phys. Oceanogr., 27: 2276-2287.

Katsman, C.A., Spall, M.A. and Pickart, R.S., 2004. Boundary current eddies and their role in the restratification of the Labrador Sea. J. Phys. Oceanogr., 34: 1967-1983.

Khatiwala, S.P. and Visbeck, M., 2000. An estimate of the eddy-induced circulation in the Labrador Sea. Geophys. Res. Lett., 27: 2277-2280.

Kraus, E.B. and Turner, J.S., 1967. A one-dimensional model of the seasonal thermocline, II, The general theory and its consequences. Tellus, 19: 98-105.

Lilly, J.M. et al., 1999. Observing deep convection in the Labrador Sea during winter 1994/95. J. Phys. Oceanogr., 29: 2065-2098.

Lilly, J.M. et al., 2003. Observations of the Labrador Sea eddy field. Prog. Oceanogr., 59: 75-176.

Lorentz, E., 1967. The Nature and Theory of the General Circulation of the Atmosphere. World Met. Org., Genève.

Madec, G., Delecluse, P., Crepon, M. and Chartier, M., 1991. A Three-Dimensional Numerical Study of Deep-Water Formation in the Northwestern Mediterranean Sea. J. Phys. Oceanogr., 21: 1349-1371.

Madec, G., P. Delecluse, M. Imbard, and C. Lévy, 1998: OPA8.1 Ocean general circulation model reference manual. Notes de l'IPSL, Université P. et M. Curie, B102 T15-E5, 4 place Jussieu, Paris cedex 5, N°11, 91p.

Marshall, J. and Schott, F., 1999. Open-ocean convection: observations, theory and models. Rev. Geophys., 37: 1-64.

Morawitz, W.M.L. et al., 1996. Three-Dimensional Observations of a Deep Convective Chimney in the Greenland Sea during Winter 1988/1989. J. Phys. Oceanogr., 26: 2316-2343.

Oort, A.H., Ascher, S.C., Levitus, S. and Peixoto, J.P., 1989. New estimates of the available potential energy in the world ocean. J. Geophys. Res., 94(C3): 3187-3200.

Pickart, R.S. and Spall, M.A., 2007. Impact of Labrador Sea Convection on the North Atlantic Meridional Overturning Circulation. Submitted to J. Phys. Oceanogr.

Send, U., Schott, F., Gaillard, F. and Desaubies, Y., 1995. Observation of a deep convection regime with acoustic tomography. J. Geophys. Res., 100 (C4): 6927-6941.

Smagorinsky, J., 1963. General circulation experiments with the primitive equations. Mon. Weather Rev., 91: 99-164.

Spall, M.A. and Chapman, D.C., 1998. On the efficiency of baroclinic eddy heat transport across narrow fronts. J. Phys. Oceanogr., 28: 2275-2287.

Thompson, L., K. A. Kelly, D. Darr, and R. Hallberg, 2002. Buoyancy and mixed-layer effects on the sea surface height response in an isopycnal model of the North Pacific. J. Phys. Oceanogr., 32: 3657-3670.

Visbeck, M., Marshall, J. and Jones, H., 1996. Dynamics of isolated convective regions in the ocean. J. Phys. Oceanogr., 26: 1721-1734.

Willebrand, J. et al., 2001. Circulation characteristics in three eddy-permitting models of the North Atlantic. Prog. Oceanogr., 48: 123-161.

Figure captions:

FIG. 1. Potential density (in ρ-1000 kg m^{-3}) distribution on the AR7W section in the Labrador Sea in 1972, as simulated by a MICOM experiment using realistic NCEP forcing (courtesy of J. Deshayes).

FIG. 2. Vertical distribution of potential density (in ρ-1000 $kg.m^{-3}$, top panels) and salinity (in pss, bottom panels) at OWS Bravo at the end of (a) March and (b) April. Thick black lines are the averaged profiles.

FIG. 3. Model configuration. (a) The model domain is a cylinder of radius $R = 250\,\mathrm{km}$ and depth $H_b = 1000\,\mathrm{m}$. (b) The initial stratification is described by 12 equally spaced layers which are uniformly distributed over the whole model domain except in a central region of radius $R_c = 70\,\mathrm{km}$ and depth $H_c = 580\,\mathrm{m}$ where the stratification is homogeneous (see explanation in text).

FIG. 4. Vertical temperature distribution (in °C) on a section through the center of the basin at selected times of the integration for (a) MICOM-ADIAB, (b) MICOM, (c) OPA.

FIG. 5. Distribution of the upper (layer 1, left panels) and deep (layer 7, right panels) layer thickness (in m) in (a) MICOM-ADIAB, (b) MICOM. (c) Distribution of temperature (in °C) at 40 m (left panel) and 290 m (right panel) in OPA. Horizontal distributions are shown as 3 day-averages around day 30. Note that in MICOM, the uppermost layer is the ML and initially contains the dense water volume.

FIG. 6. Time evolution of the relative change of buoyancy $\frac{B(t) - B(t=0)}{B(t=0)}$ integrated over the whole water column in the central part (cylinder of radius 70 km) of the domain for MICOM-ADIAB (red), MICOM (green) and OPA (black). The additional dashed green curve represents the "imposed-retreat" experiment.

FIG. 7. Time evolution of the volume of each isopycnic layer in the central (cylinder of radius 70 km) (solid line, left axis) and outer (dashed line, right axis) regions for the four simulations shown in fig. 6. Volumes are normalized by the surface of the convective patch so as to represent thicknesses (in m). Dotted lines are used for MICOM as long as the properties of the "layer" do not match that of the corresponding isopycnic layer (see explanation in text). Colours as in figure 6.

FIG. 8. Horizontal velocity (in cm s^{-1}) averaged over (a) the uppermost 83 m, and (b) the layer 500-583 m, on day 30 in MICOM-ADIAB.

FIG. 9. Vertical distribution of the eddy kinetic energy (in 10^6 J m^{-2}) as a function of the distance to the centre of the basin for (a) MICOM-ADIAB (b) MICOM and (c) OPA. Energy values are obtained through azimuthal integration. Note that energies plotted in (b) have been multiplied by 3.

FIG. 10. Time-depth distribution of the eddy kinetic energy (in J m^{-2}) averaged over the whole basin area for (a) MICOM-ADIAB, (b) MICOM, and (c) OPA.

FIG. 11. Time evolution of the vertically (top to bottom) integrated mean (solid line) and eddy (dashed line), kinetic (thin line) and available potential (bold line) energies averaged over the whole basin area (in J m^{-2}) for (a) MICOM-ADIAB (b) MICOM, and (c) OPA. The right axis corresponds to the mean available potential energy in the three models and also to the eddy available potential energy in MICOM. The left axis corresponds to the other energies.

FIG. 12. Time evolution of the vertically (top to bottom) integrated energy conversion rates averaged over the whole basin area (in W m^{-2}) for (a) MICOM-ADIAB, and (b) OPA. $C(P,K_M)$ in red, $C(P,K_E)$ in blue, $C(K_M,K_E)$ in green. Dashed red (resp. blue) line corresponds to the change in mean (resp. eddy) kinetic energy due to viscosity.

FIG. 13. Vertical distribution of $\partial q/\partial r$ (in 10^{-15} m^{-2} s^{-1}) as a function of the distance to the centre of the basin on days 12 and 30 for (a) MICOM ADIAB, (b) MICOM, and (c) OPA. Also shown in (d) is the vertical distribution of the local contribution $-g\overline{hw'\rho'}$ to the conversion rate $C(P,K_E)$ in OPA on day 30. q is the potential vorticity associated with the mean flow. In MICOM-ADIAB and MICOM, the layer expression of q, (18), is multiplied by $\Delta\rho$, the density jump between the model layers.

FIG. 14. Vertical distribution of the azimuthally integrated horizontal eddy mass flux (in 10^3 m^2 s^{-1}) as a function of the distance to the centre of the basin for (a) MICOM-ADIAB and (b) MICOM.

FIG. 15. Time-radial distance distribution of the azimuthally integrated contributions to the change in ML heat content (in 10^9 W m^{-1}) in MICOM: (a) mass flux convergence, (b) hydrostatic instability, (c) temperature advection, (d) sum of the three contributions. Also shown in (e) is the heat flux convergence integrated over the whole water column. In (a), (b) and (d) the scale should be multiplied by 10.

FIG. 16. Vertical distribution of the azimuthally integrated horizontal eddy heat fluxes (in 10^6 W m^{-2}) for (a) MICOM-ADIAB, (b) MICOM, and (c) OPA.

FIG. 17. Time-radial distance distribution of the azimuthally and vertically integrated convergence of the eddy heat fluxes (in 10^9 W m^{-1}) for (a) MICOM-ADIAB, and (b) OPA.

FIG. 18. Horizontal distribution of relative vorticity (in 10^{-4} s^{-1}, coloured scale) on day 30 (left two panels) and distribution of relative vorticity and temperature (°C) on a section through the centre of the basin on day 20 (right two panels) for (a) MICOM-ADIAB and (b) OPA. In the left panels, vorticity is plotted (a) for the uppermost (layer 1) and dense (layer 7) layers superimposed with isolines of the corresponding layer thickness and (b) at selected depth levels (40 m and 375 m) superimposed with isolines of the temperature (°C).

Cover Letter

A multi-model study of the restratification phase in an idealized convection basin

Clément Rousset [a*], Marie-Noëlle Houssais [a], Eric P. Chassignet [b]

[a] LOCEAN-IPSL, UMR 7159, Université Paris 6, 4 Place Jussieu, Paris, France
[b] Center for Ocean-Atmospheric Prediction Studies, Florida State University, Tallahassee, FL, USA.

Submitted to *Ocean Modelling*

November 1, 2007

* Corresponding author address: LOCEAN-IPSL, UMR 7159, Université Paris 6, Boîte 100, 4 Place Jussieu, 75005 Paris, France.

Tel: (+33)1-44-27-70-71. Fax: (+33)1-44-27-38-05

E-mail address: clement.rousset@locean-ipsl.upmc.fr (Clément Rousset)

Figure

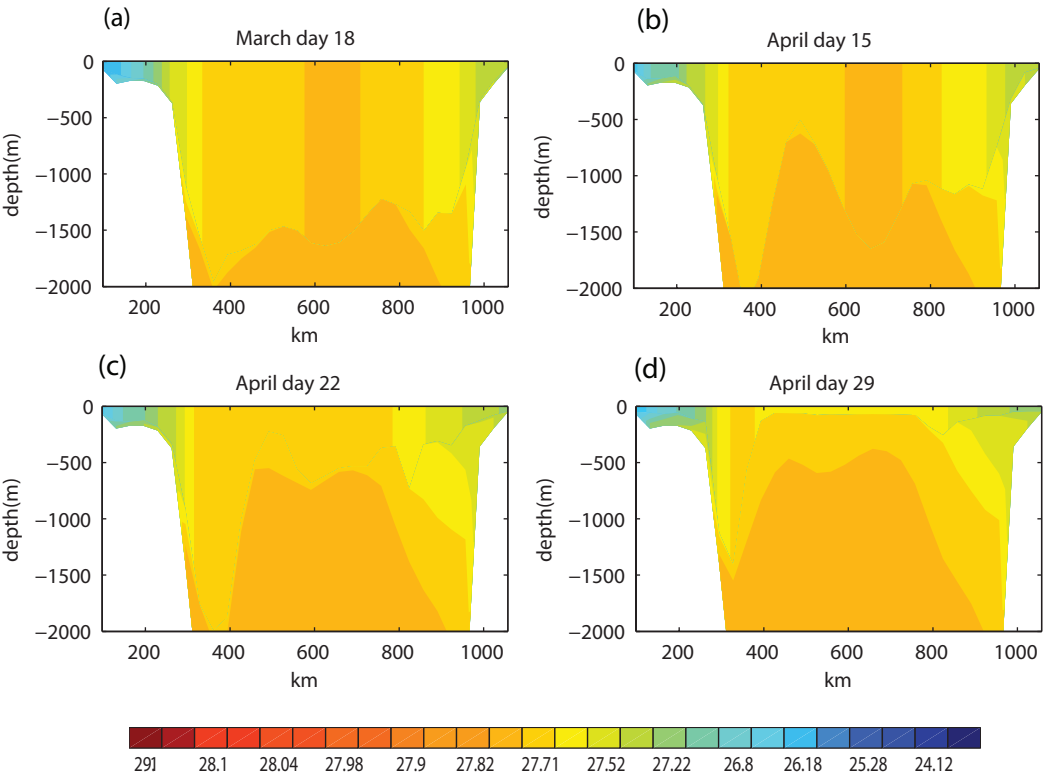
(a)
March day 18
(b)
April day 15
(c)
April day 22
(d)
April day 29
depth(m)
0
−500
−1000
−1500
−2000
200
400
600
800
1000
km
291
28.1
28.04
27.98
27.9
27.82
27.71
27.52
27.22
26.8
26.18
25.28
24.12

Figure

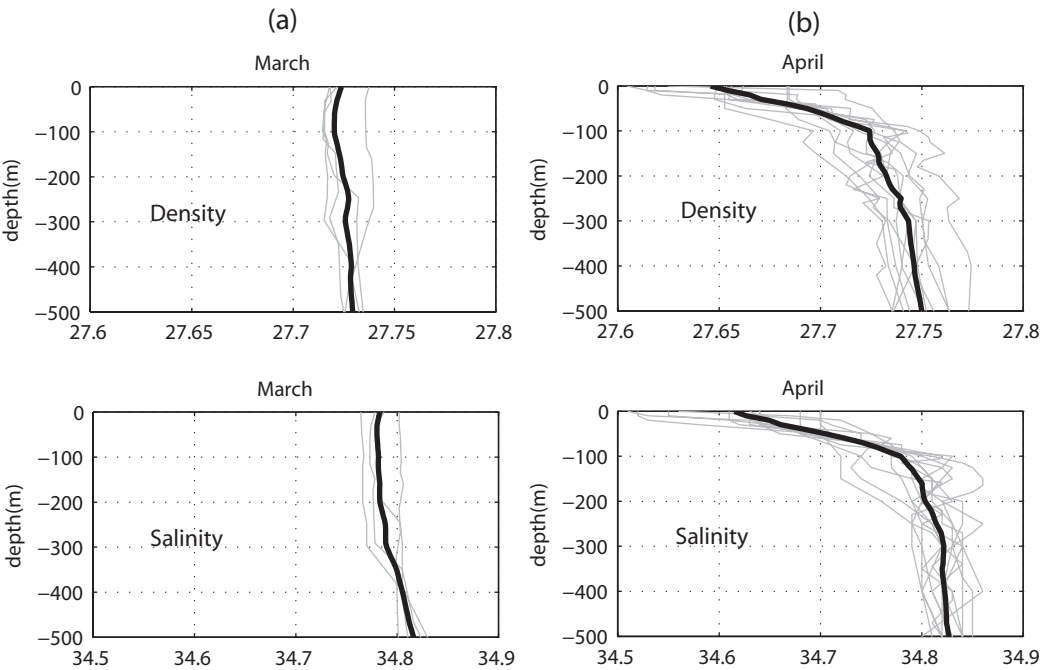
(a)
March
Density
depth(m)
0
−100
−200
−300
−400
−500
27.6
27.65
27.7
27.75
27.8
March
Salinity
depth(m)
34.5
34.6
34.7
34.8
34.9
(b)
April
Density
depth(m)
April
Salinity
depth(m)

Figure

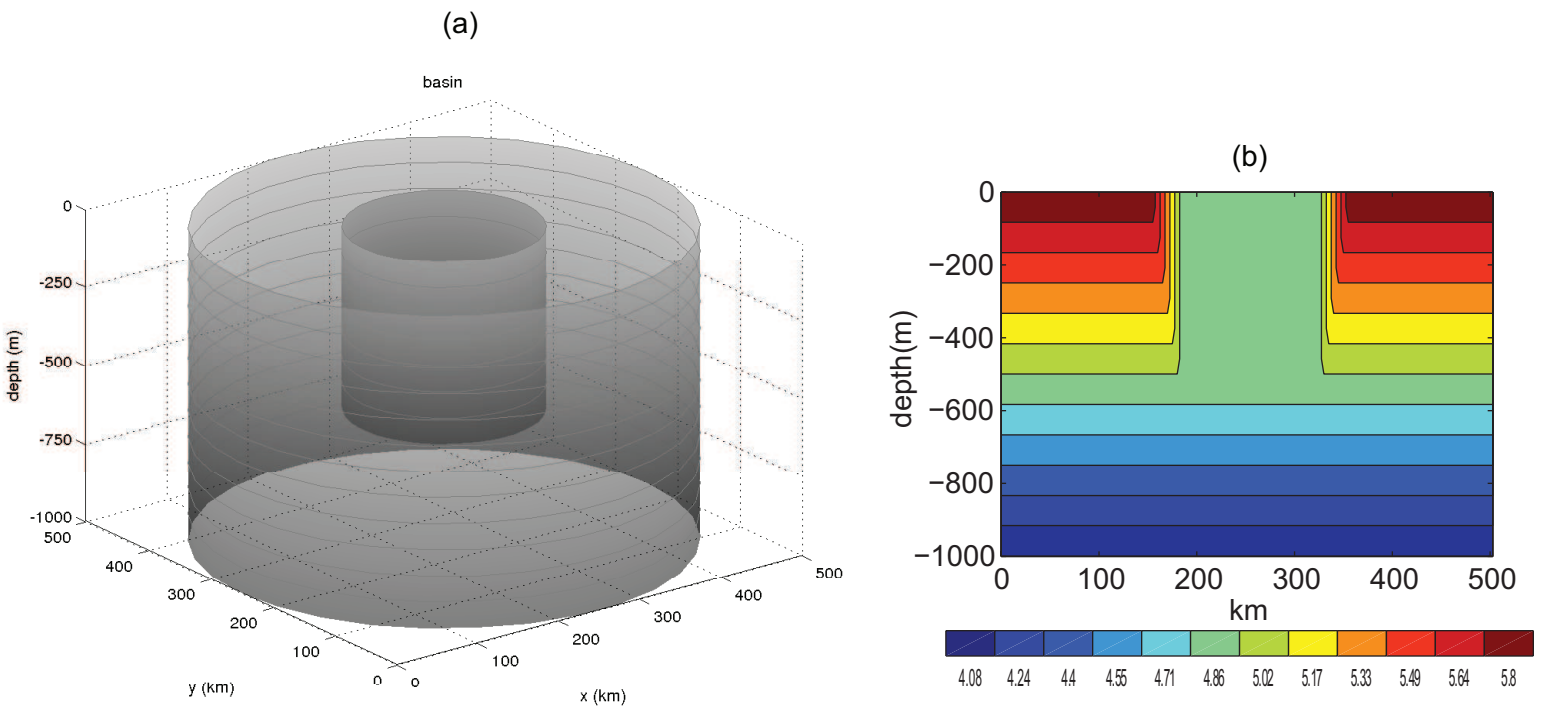
(a)
basin
depth (m)
0
-250
-500
-750
-1000
500
400
300
200
100
0
y (km)
0
100
200
300
400
500
x (km)
(b)
depth(m)
0
−200
−400
−600
−800
−1000
0
100
200
300
400
500
km
4.08
4.24
4.4
4.55
4.71
4.86
5.02
5.17
5.33
5.49
5.64
5.8

Figure

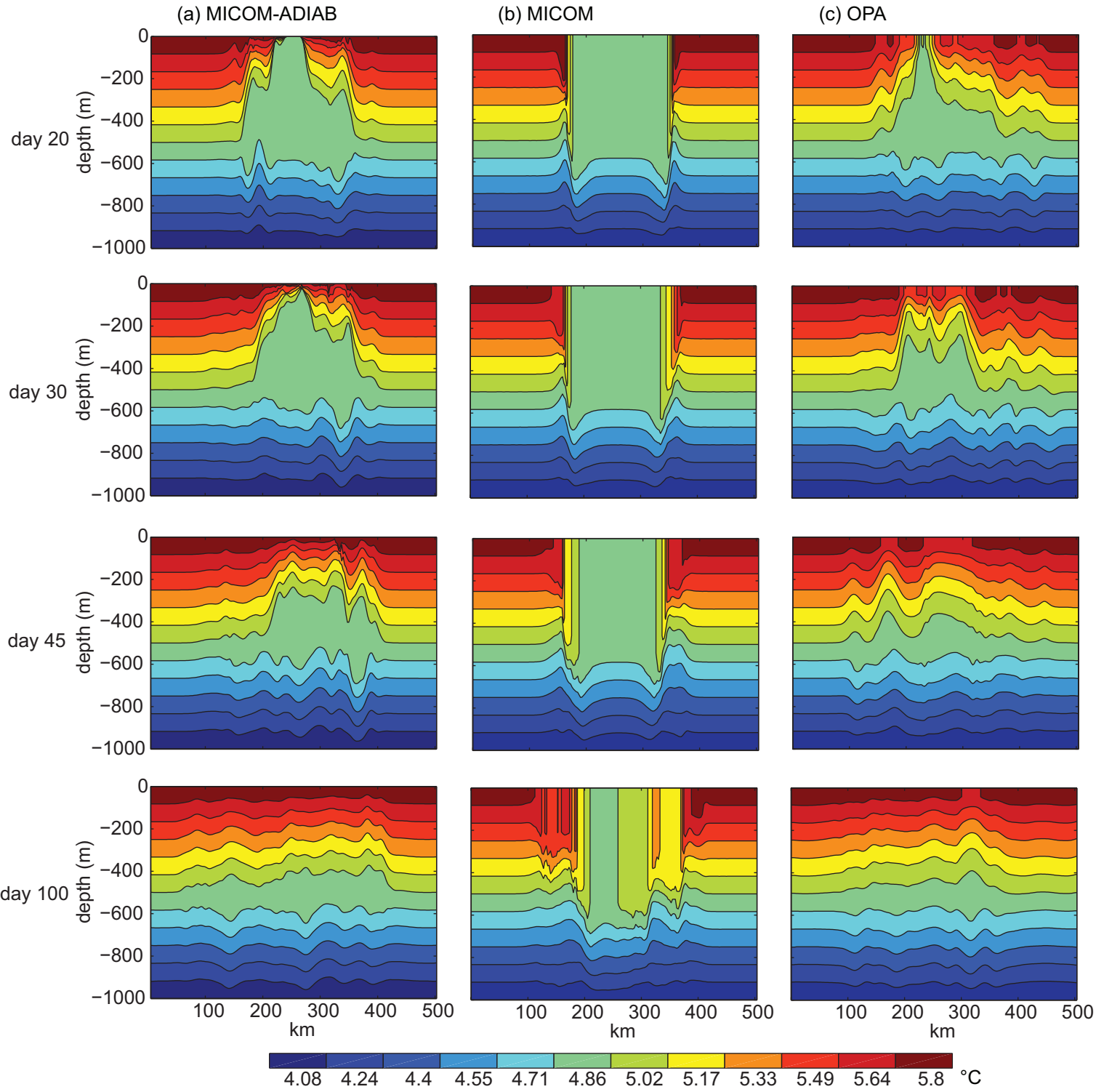
(a) MICOM-ADIAB
(b) MICOM
(c) OPA
day 20
day 30
day 45
day 100
depth (m)
0
−200
−400
−600
−800
−1000
100
200
300
400
500
km
4.08
4.24
4.4
4.55
4.71
4.86
5.02
5.17
5.33
5.49
5.64
5.8
°C

Figure

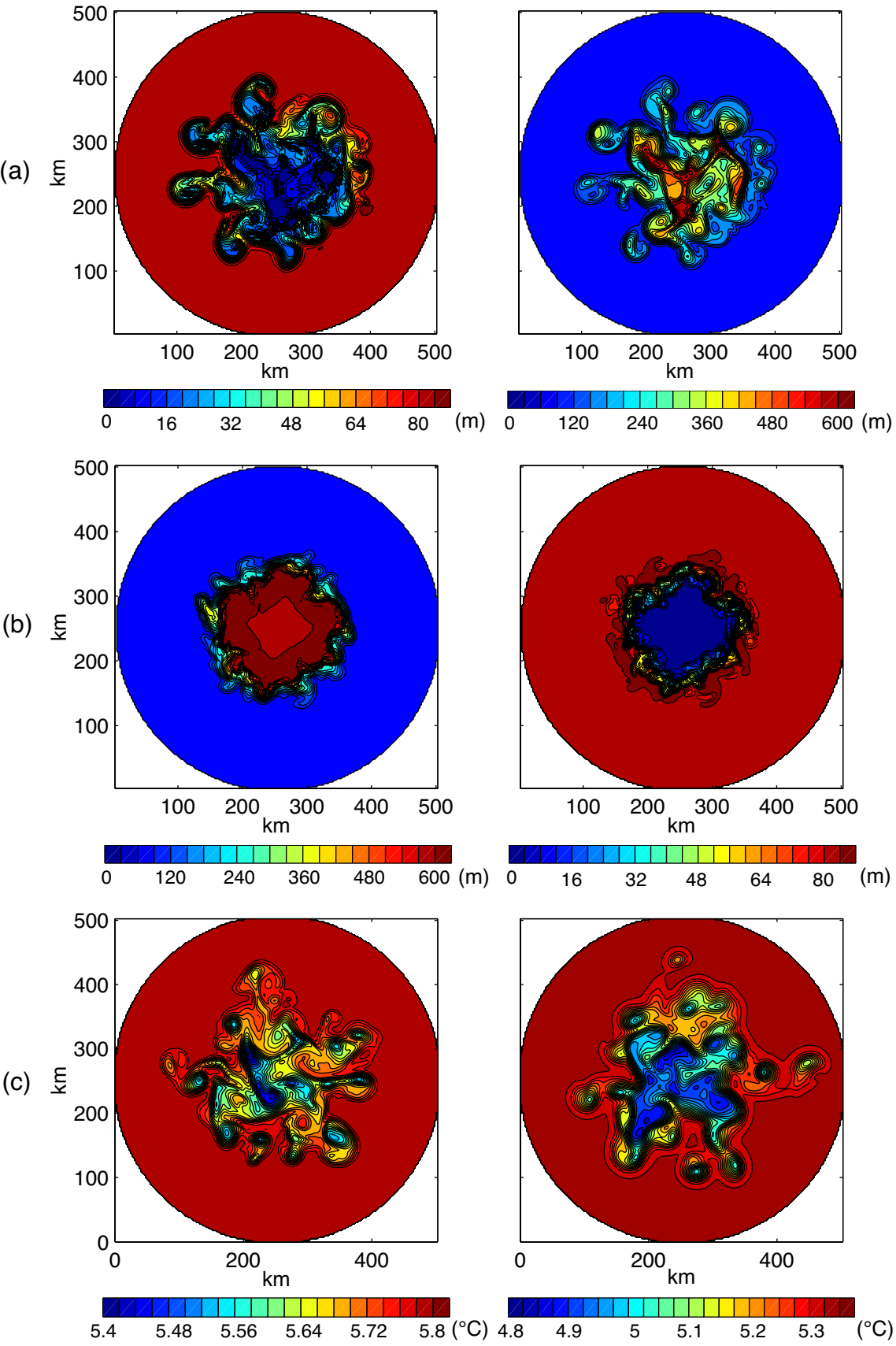
(a)
500
400
300
200
100
km
100 200 300 400 500
km
0 16 32 48 64 80 (m)
0 120 240 360 480 600 (m)
(b)
0 120 240 360 480 600 (m)
0 16 32 48 64 80 (m)
(c)
0
0 200 400
5.4 5.48 5.56 5.64 5.72 5.8 (°C)
4.8 4.9 5 5.1 5.2 5.3 (°C)

Figure

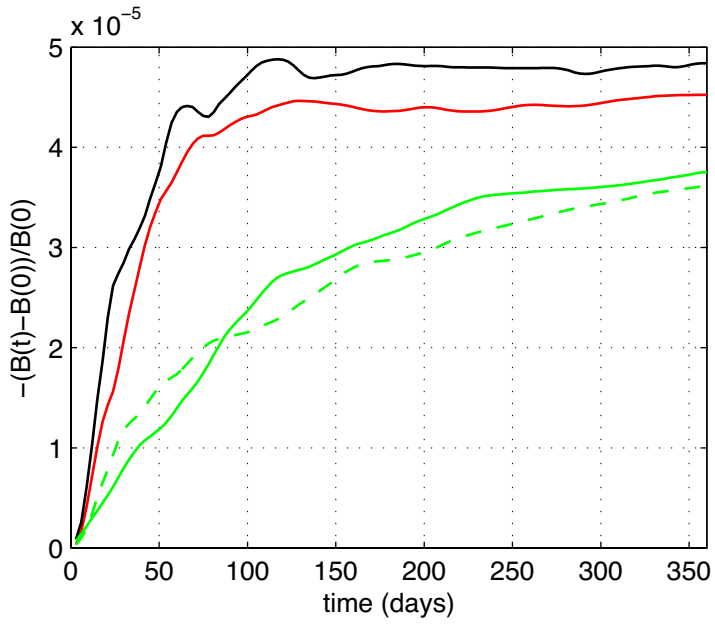

Figure

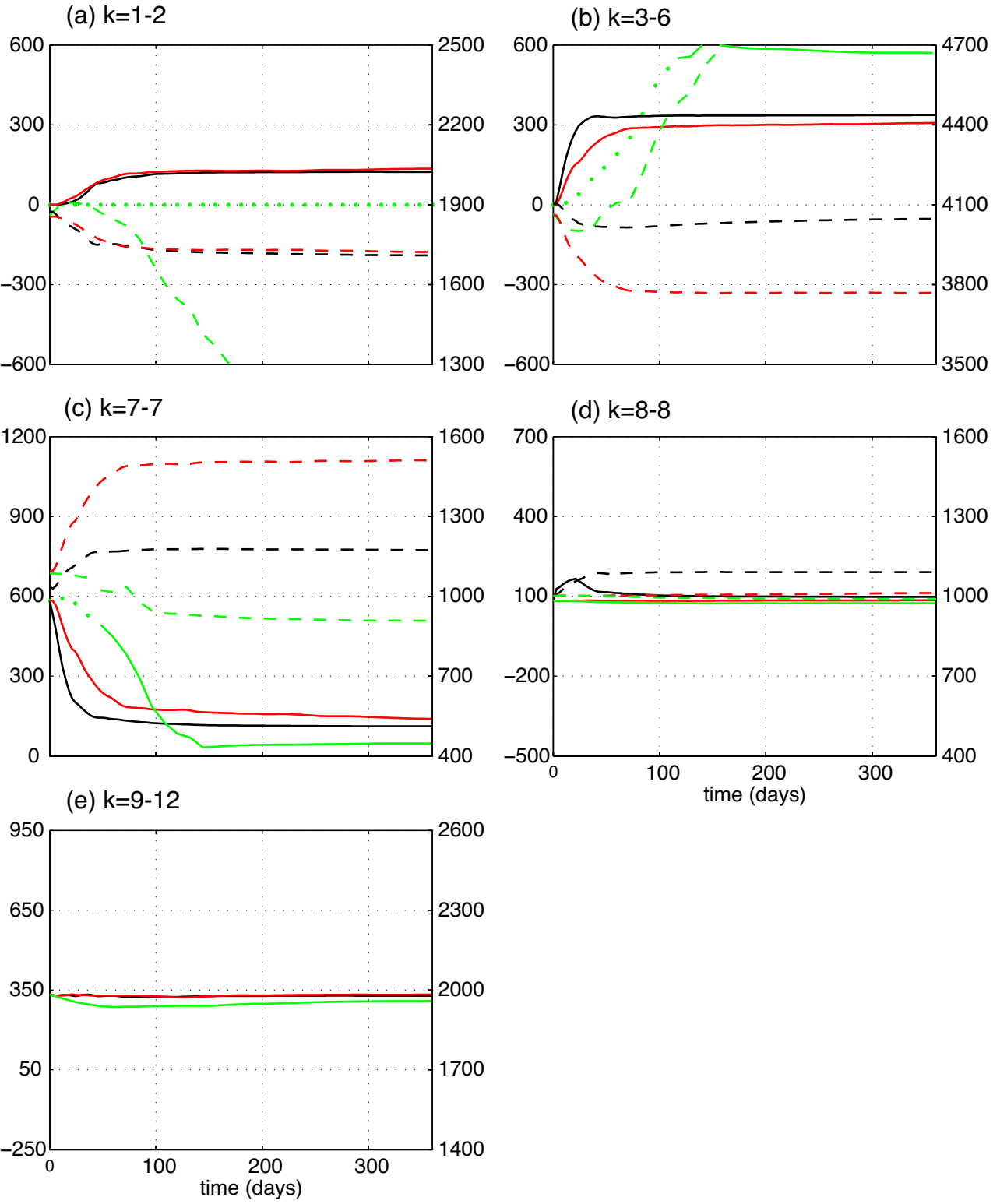
(a) k=1-2
600
300
0
−300
−600
2500
2200
1900
1600
1300
(b) k=3-6
600
300
0
−300
−600
4700
4400
4100
3800
3500
(c) k=7-7
1200
900
600
300
0
1600
1300
1000
700
400
(d) k=8-8
700
400
100
−200
−500
1600
1300
1000
700
400
0
100
200
300
time (days)
(e) k=9-12
950
650
350
50
−250
2600
2300
2000
1700
1400
0
100
200
300
time (days)

Figure

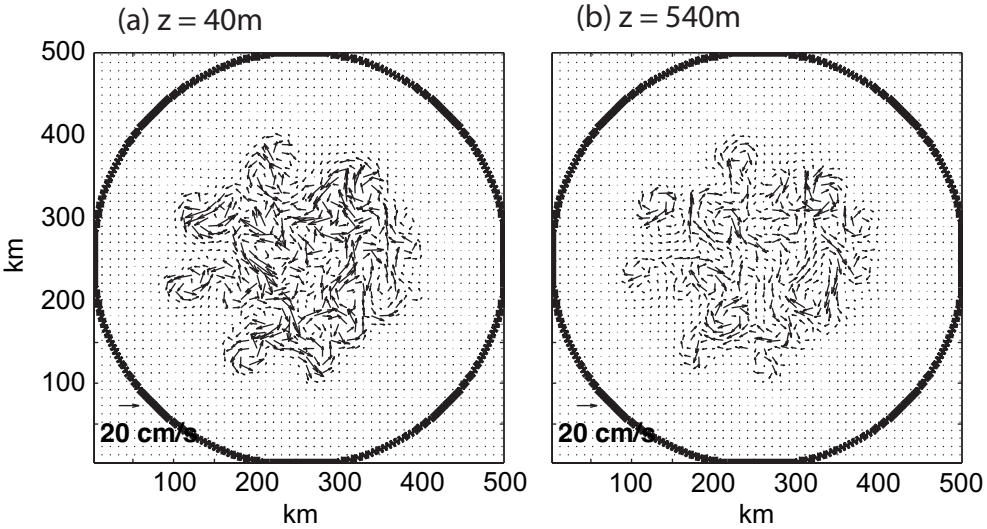
(a) z = 40m
(b) z = 540m
500
400
300
200
100
km
20 cm/s
20 cm/s
100
200
300
400
500
km

Figure

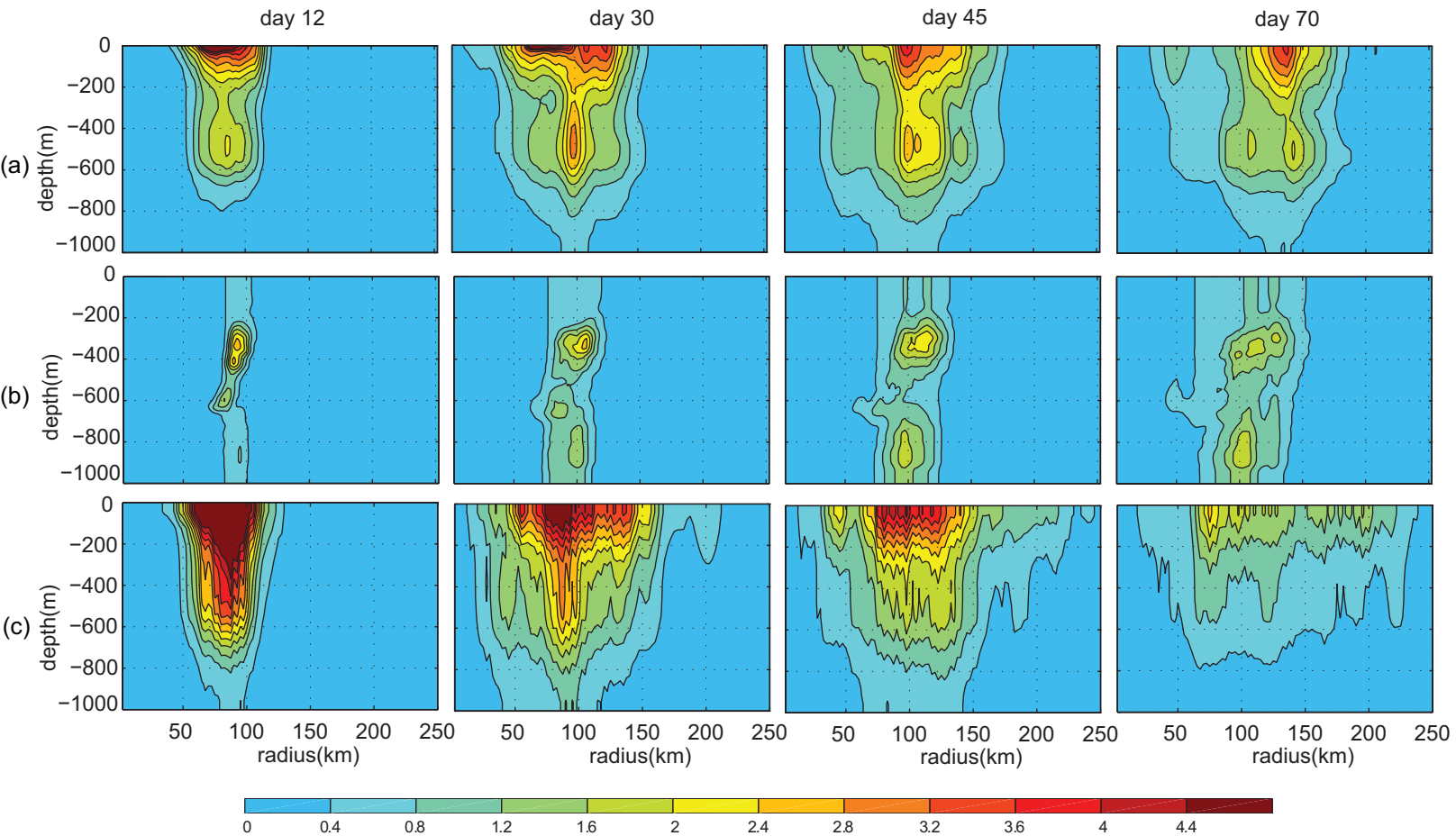
day 12
day 30
day 45
day 70
(a)
(b)
(c)
depth(m)
0
−200
−400
−600
−800
−1000
50
100
150
200
250
radius(km)
0
0.4
0.8
1.2
1.6
2
2.4
2.8
3.2
3.6
4
4.4

Figure

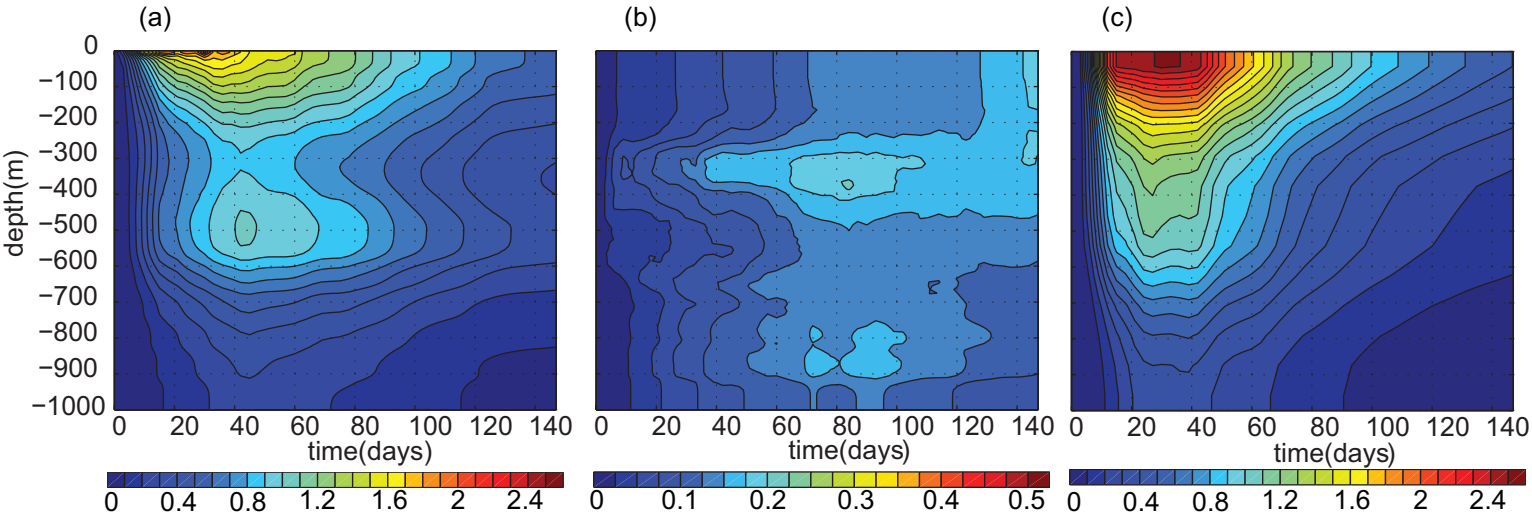
(a)
(b)
(c)
depth(m)
0
−100
−200
−300
−400
−500
−600
−700
−800
−900
−1000
0 20 40 60 80 100 120 140
time(days)
0 0.4 0.8 1.2 1.6 2 2.4
0 0.1 0.2 0.3 0.4 0.5

Figure

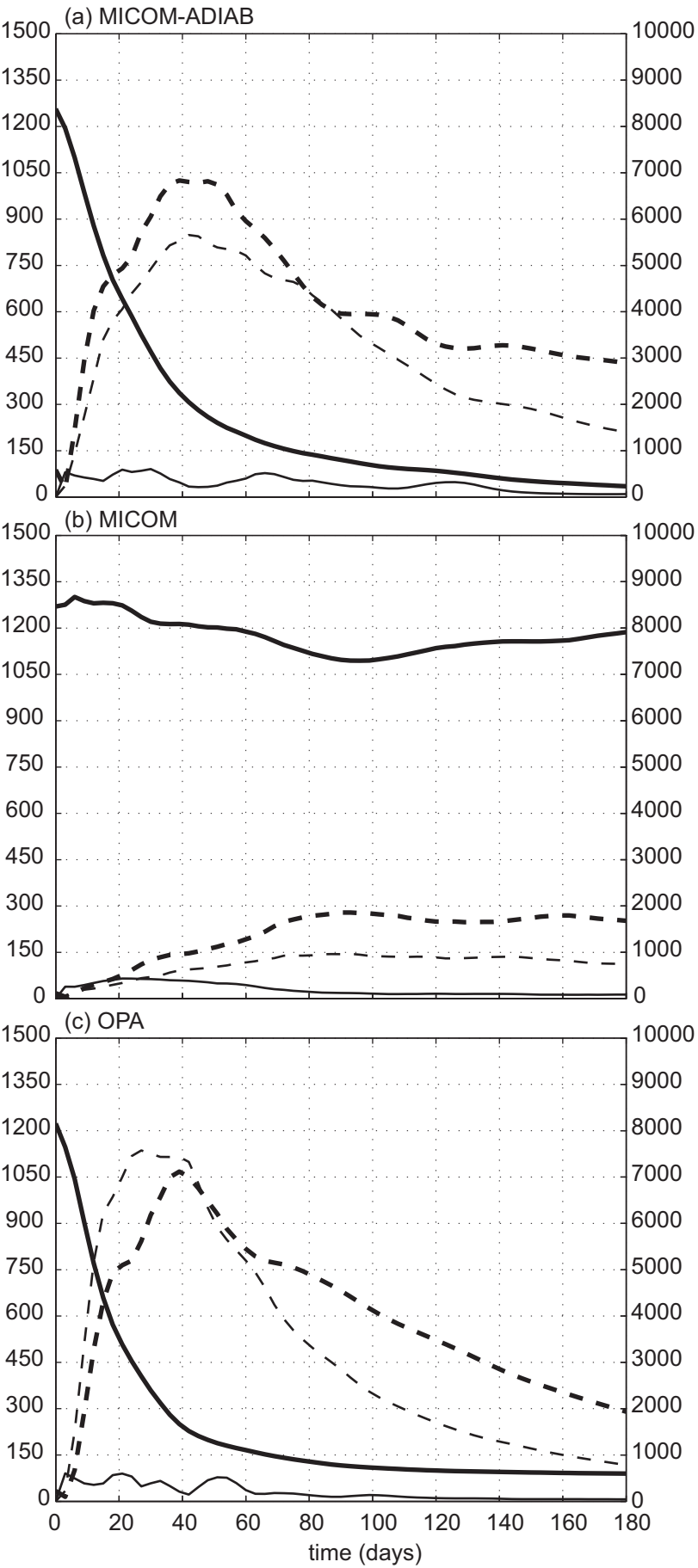
(a) MICOM-ADIAB
(b) MICOM
(c) OPA
1500
1350
1200
1050
900
750
600
450
300
150
0
10000
9000
8000
7000
6000
5000
4000
3000
2000
1000
0
0
20
40
60
80
100
120
140
160
180
time (days)

Figure

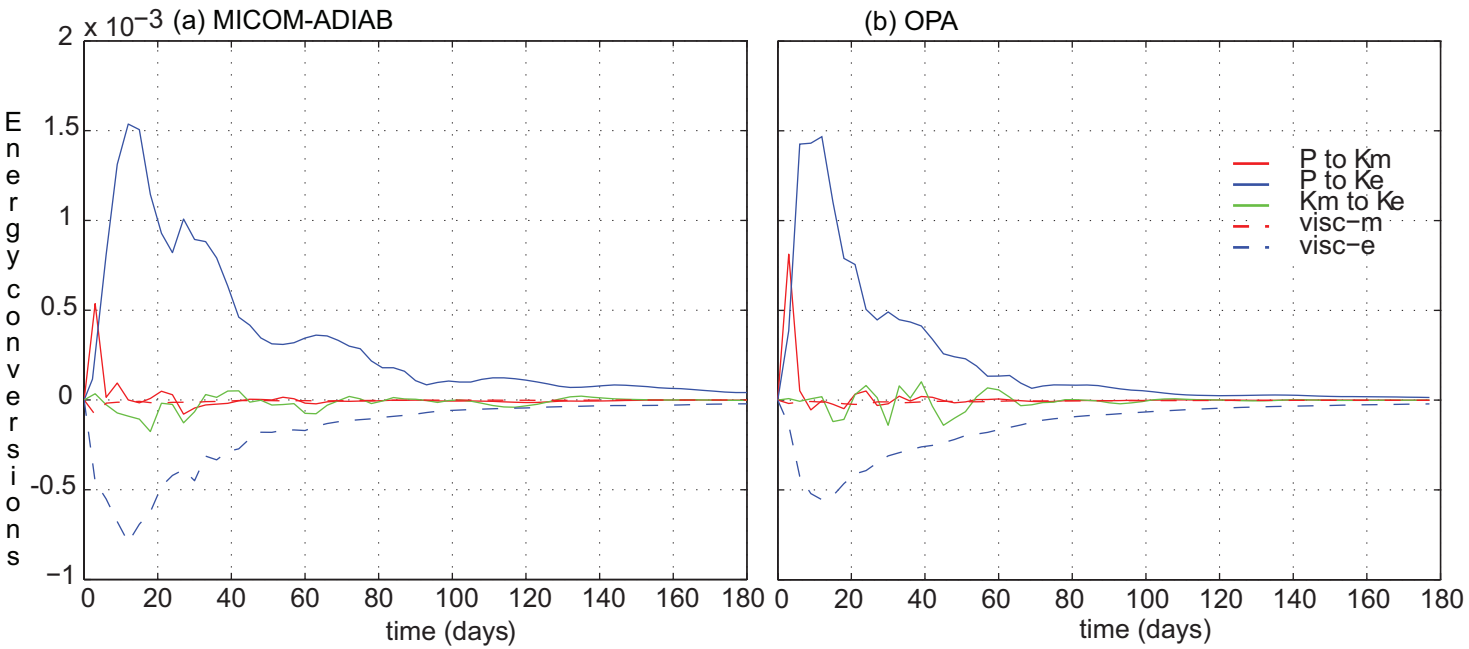
(a) MICOM-ADIAB
(b) OPA
x 10−3
2
1.5
1
0.5
0
-0.5
−1
Energy conversions
0
20
40
60
80
100
120
140
160
180
time (days)
P to Km
P to Ke
Km to Ke
visc−m
visc−e

Figure

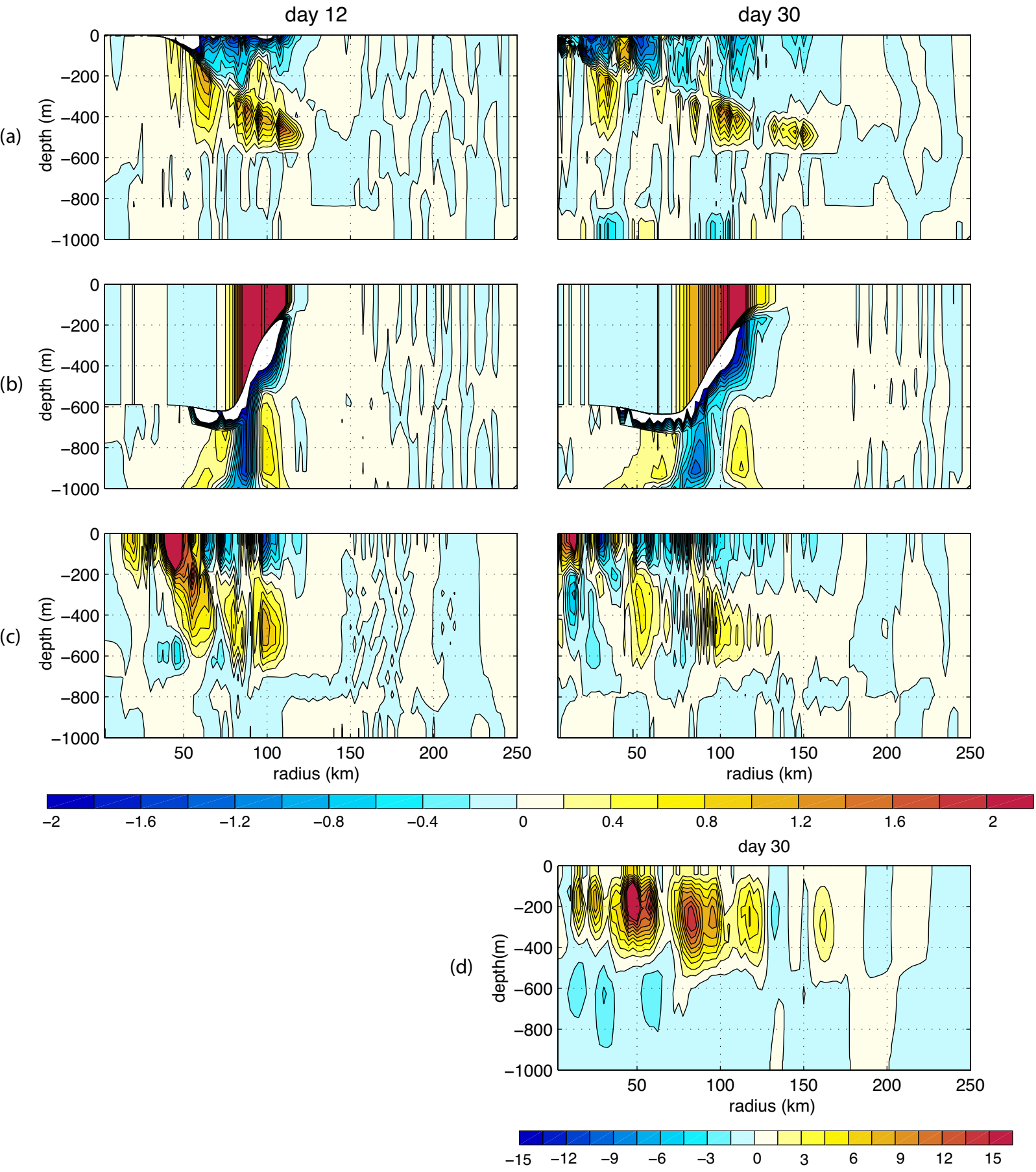
day 12
day 30
(a)
(b)
(c)
(d)
depth (m)
depth(m)
0
−200
−400
−600
−800
−1000
50
100
150
200
250
radius (km)
−2
−1.6
−1.2
−0.8
−0.4
0
0.4
0.8
1.2
1.6
2
−15
−12
−9
−6
−3
0
3
6
9
12
15

Figure

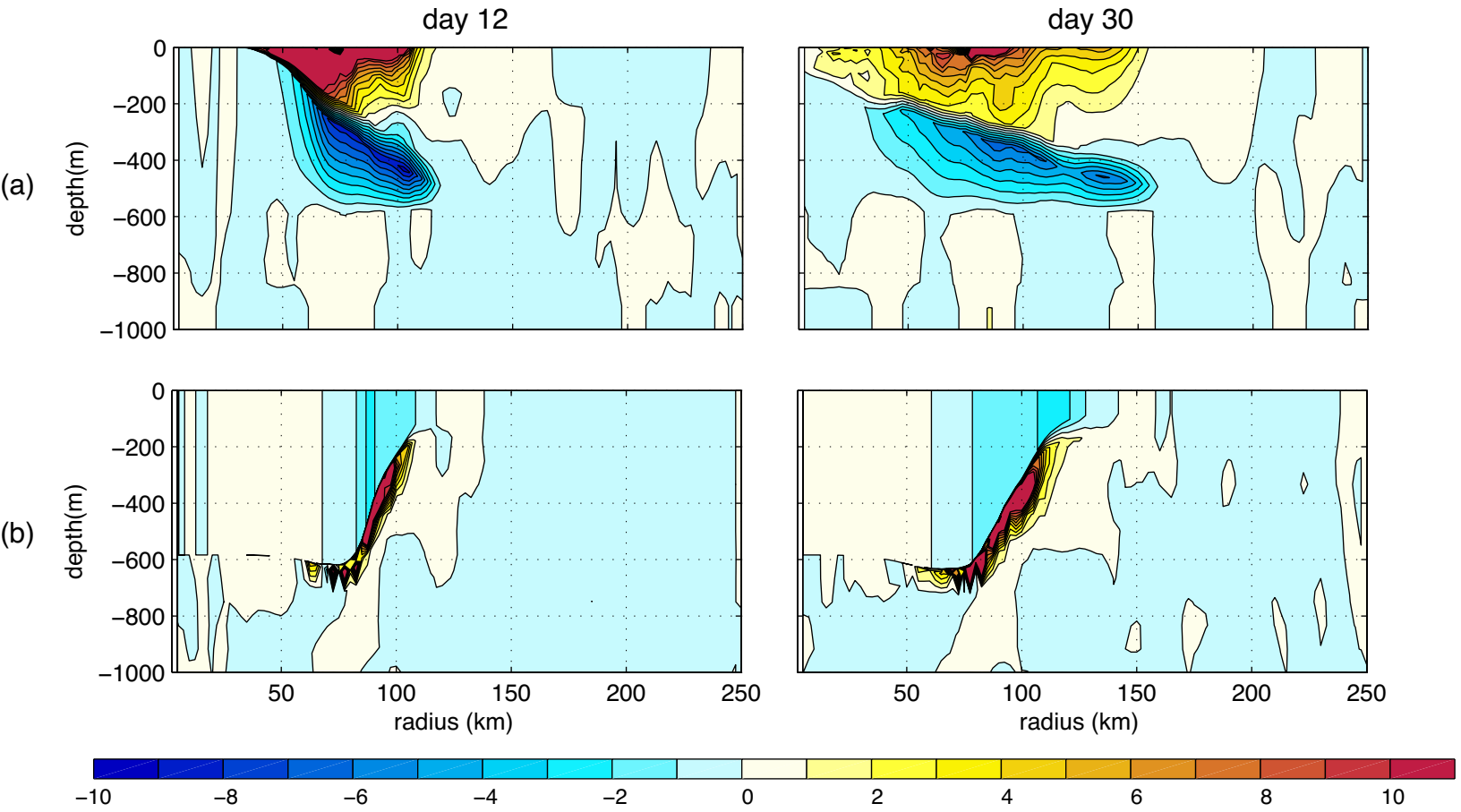
day 12
day 30
(a)
(b)
depth(m)
0
−200
−400
−600
−800
−1000
50
100
150
200
250
radius (km)
−10
−8
−6
−4
−2
0
2
4
6
8
10

Figure

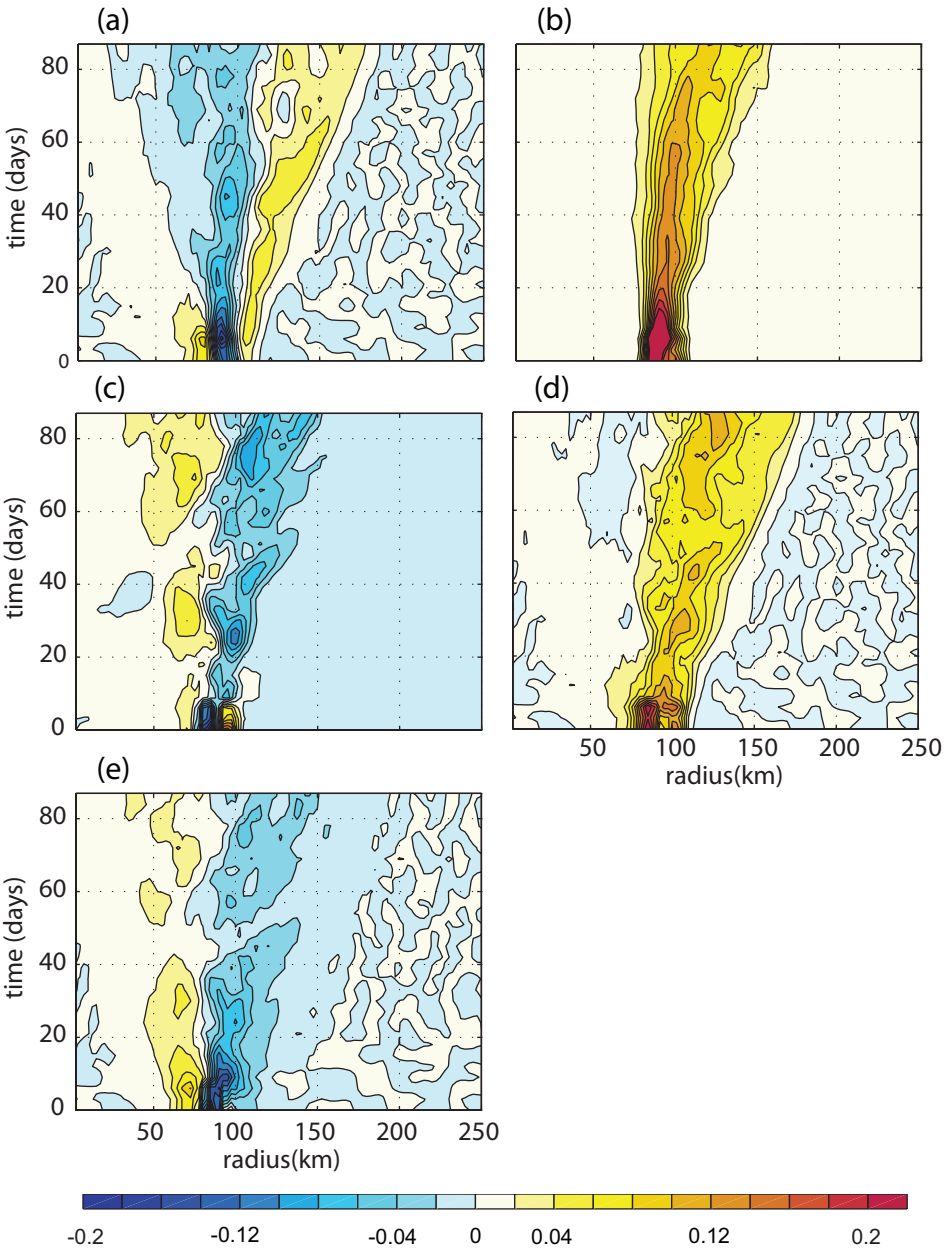
(a)
(b)
(c)
(d)
(e)
time (days)
0
20
40
60
80
50
100
150
200
250
radius(km)
-0.2
-0.12
-0.04
0
0.04
0.12
0.2

Figure

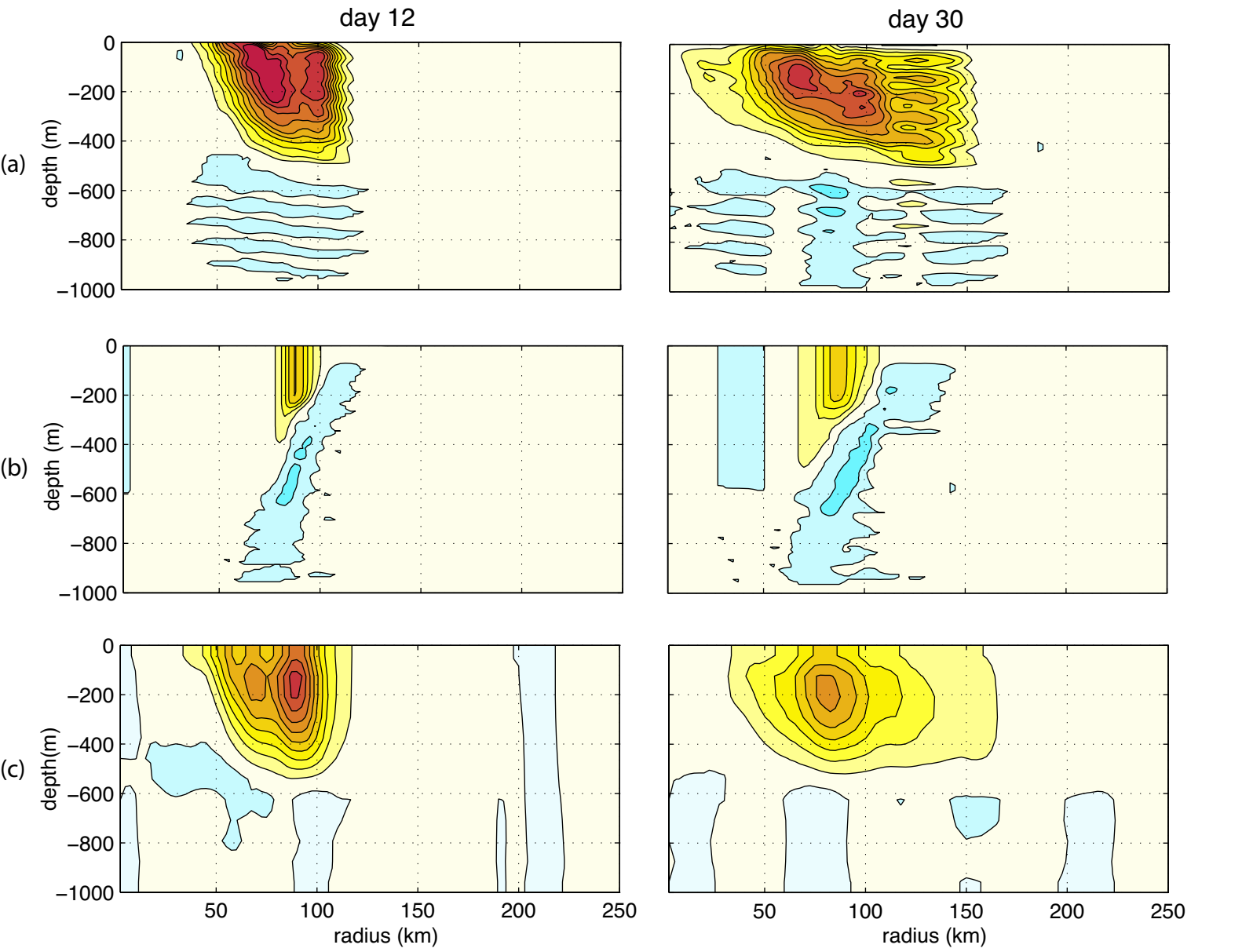
day 12
day 30
(a)
(b)
(c)
depth (m)
depth(m)
0
−200
−400
−600
−800
−1000
50
100
150
200
250
radius (km)
−20
−16
−12
−8
−4
0
4
8
12
16
20

Figure

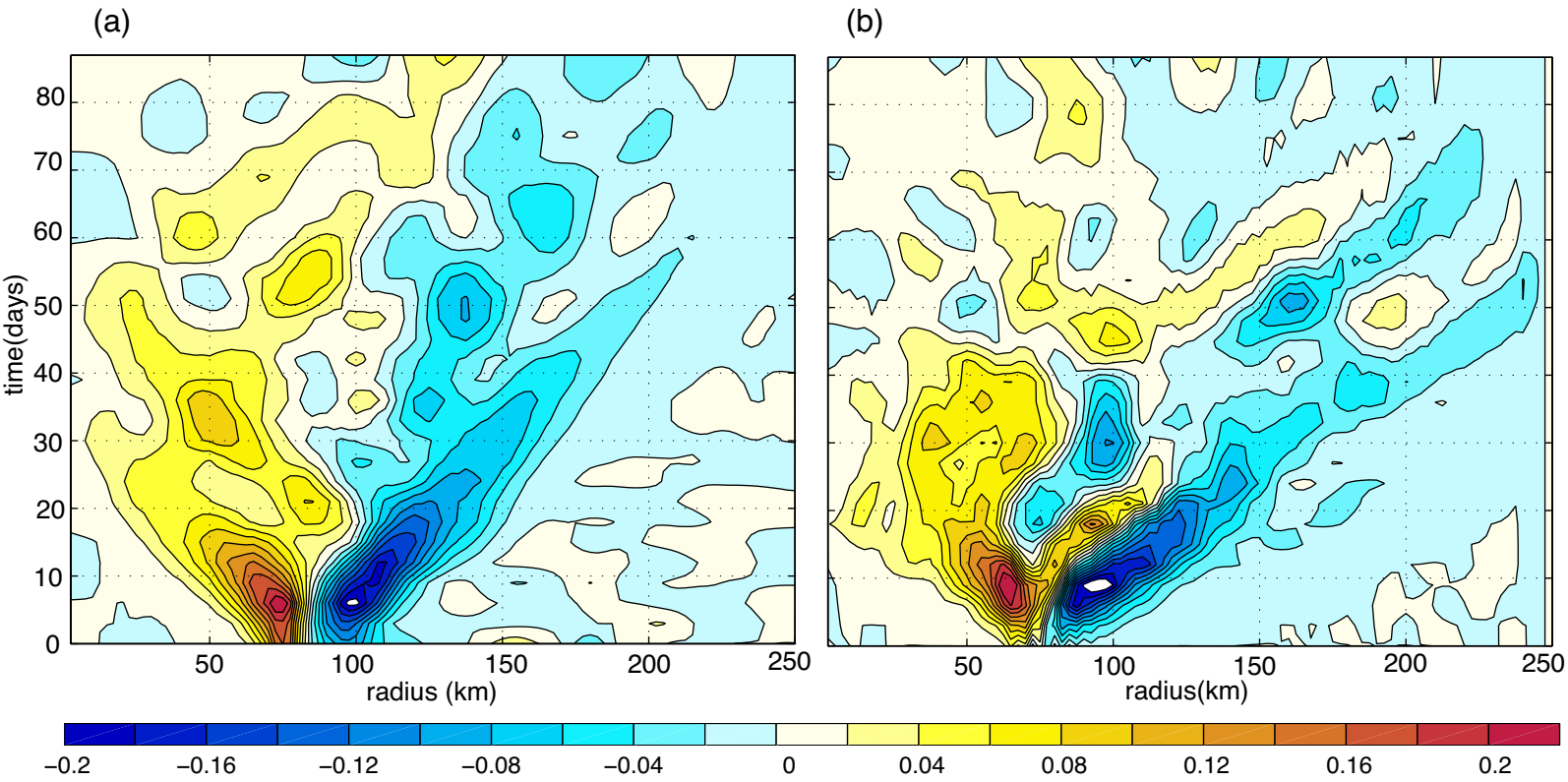
(a)
(b)
time(days)
0
10
20
30
40
50
60
70
80
50
100
150
200
250
radius (km)
radius(km)
−0.2
−0.16
−0.12
−0.08
−0.04
0
0.04
0.08
0.12
0.16
0.2

Figure

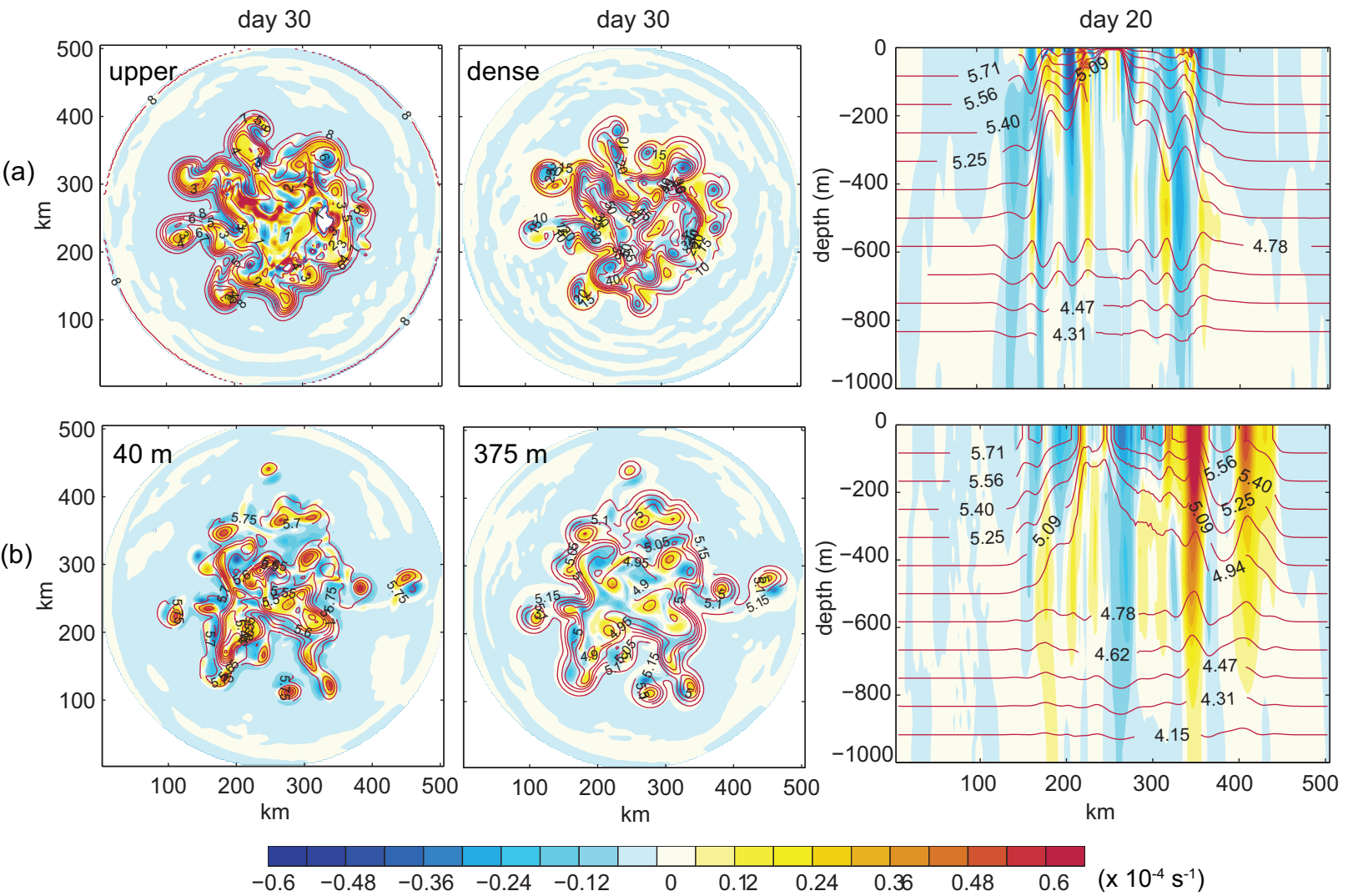
day 30
day 30
day 20
(a)
upper
dense
km
depth (m)
5.71
5.56
5.40
5.25
5.09
4.78
4.47
4.31
(b)
40 m
375 m
km
depth (m)
5.71
5.56
5.40
5.25
5.09
4.94
4.78
4.62
4.47
4.31
4.15
100
200
300
400
500
0
−200
−400
−600
−800
−1000
−0.6
−0.48
−0.36
−0.24
−0.12
0
0.12
0.24
0.36
0.48
0.6
(x 10-4 s-1)